$\cdot Si \equiv Si_3$ defect at thermally grown (111)Si/Si_3N_4 interfaces

A. Stesmans and G. Van Gorp
Department of Physics, Universiteit Leuven, 3001 Leuven, Belgium
(Received 7 February 1995)

Electron-spin resonance on various dehydrogenated (111)Si/(oxy)nitride structures, thermally grown at 1000–1150 °C in NH_3, reveals the presence of two defects. The major one, called P_{bN}, is identified as a Si dangling bond ($\cdot Si \equiv Si_3$) at the (111)Si/nitride interface aligned perpendicular to the interface; x-ray photoelectron spectroscopy actually shows that the *in situ* removal of the native Si oxide prior to nitridation is a prerequisite to obtaining stoichiometric Si_3N_4 films. The identification is based on strong similarities with the P_b defect at the (111)Si/SiO_2 interface, such as the g matrix, the location at the interface, and linewidth anisotropy. This observation of the $\cdot Si \equiv Si_3$ defect at a natural Si/solid interface other than the Si/SiO_2 one confirms P_b as a prototype dangling-bond center, its salient properties being set by the underside Si matrix—not by the overlaying insulator. Yet, secondary ESR signatures do differ as the large interface strain, resulting from the greater rigidity of the (oxy)nitrides as compared to SiO_2 films, causes a slight perturbation of the $P_{b(N)}$ symmetry, thereby lifting its C_{3v} symmetry. This is born out at 4.3 K by specific distortions of the P_{bN} line shape. Upon increasing temperature, the perturbation of the defect's symmetry is smoothed due to thermally activated averaging over the various defect distortions. The properties of the P_b and P_{bN} defects at higher temperatures become largely identical. Comparison of the extracted unresolved ^{14}N P_{bN} and ^{17}O P_b hf broadenings shows that their relative strengths comply with the known isotopic properties. A second defect, the intrinsic K center ($\cdot Si \equiv N_3$), with isotropic $g = 2.0028 \pm 0.0001$, is observed only in stoichiometric Si_3N_4 films.

I. INTRODUCTION

The study of a-Si_3N_4 films on c-Si has gained widespread interest during recent years. Indeed, as devices keep scaling down,[1] the higher density, higher dielectric constant,[2] and promising radiation hardness[3] of a-Si_3N_4 as compared to a-SiO_2, together with its application as a very efficient diffusion barrier,[4] make it a desirable material in semiconductor technology. The electronic properties of a-Si_3N_4 are dominated by deep traps, which were extensively studied electrically over the past two decades.[5,6] In search of their atomic identity, electron-spin resonance (ESR) studies on a-Si_3N_4 films, prepared in a variety of ways, revealed two signals of zero crossing, $g \approx 2.003$ and $g \approx 2.006$, respectively. Observation of hyperfine (hf) structure allowed conclusive identification of a dangling sp^3-hybrid orbital[7] on a Si atom backbonded to three N atoms (K center; $\cdot Si \equiv N_3$), and a dangling p orbital[8] located on a probably twofold-coordinated N atom ($\cdot N \equiv Si_2$), respectively. (For a comprehensive review on these centers, see Ref. 9.) The K center[10] was shown to account for the majority of traps measured electrically.

While the main research efforts address the bulk properties of a-Si_3N_4, the characterization of the c-Si/Si_3N_4 structure may appear equally important, not in the least because it provides a unique system to conduct a fundamental comparative study of localized states at different interfaces between c-Si and Si-based thermally grown insulators. The dominant defect—in effect the only one so far identified at the (111)Si/SiO_2 interface—is the $\cdot Si \equiv Si_3$ defect. As observed by ESR (neutral, paramagnetic state), it is termed the P_b defect and accounts for at least half of the interface states observed electrically.[11] Based on the defect's C_{3v} symmetry with attendant axially symmetric $\overleftrightarrow{g}$ matrix of principal values[12] $g_\parallel = 2.0013 \pm 0.0001$ ($\sim$ the free-electron value $g_0 = 2.002\,319$) and $g_\perp = 2.0087 \pm 0.0003$ ($g_\perp > g_0$), the linewidth anisotropy,[13] and the observation of the (super)hf signals,[14,15] the wave function of the unpaired P_b electron was shown to consist primarily of a sp^3-hybrid orbital on an interfacial Si atom, backbonded to three Si atoms in the substrate and pointing into a microvoid. The center is also responsible for the majority of interface defects at the (100)Si/SiO_2 interface.[16] In conventionally grown ($\sim$1 atm O_2, $\sim$950 °C) (111)Si/SiO_2 structures, only the variant with the unpaired sp^3 hybrid along [111] (perpendicular to the interface)—the [111] P_b defect—is observed. In poor-quality structures, the species with the unpaired bond along the equivalent $[\bar{1}11]$, $[1\bar{1}1]$, or $[11\bar{1}]$ direction—the 19° P_b centers—are also observed.[17,18]

Several questions about P_b centers remain, such as the essence of their generation kinetics during or after the insulator's growth, and their interaction with the surrounding lattice. Therefore, it might prove useful to study the P_b defect in different environments, such as when placed at the native SiO_2/Si interface,[18] near a buried SiO_2/Si interface,[15] or at another thermally grown natural insulator/(111)Si interface.[19] The present study extends previous ESR work on P_b toward the Si/Si_3N_4 interface: It is hoped in this way to obtain useful information about the P_b defect and related interface structure, otherwise inaccessible when sticking to the (111)Si/SiO_2 interface.

A brief account of the P_b-type defect observation in

0163-1829/95/52(12)/8904(17)/$06.00

thermal Si/Si$_3$N$_4$ has been given previously.[20] The objective of this work is a fundamental exploration of this defect, based on the detailed analysis of its ESR features in combination with varying nitridation parameters.

II. EXPERIMENTAL TECHNIQUES

A. Sample preparation

Samples were routinely prepared from 3-in Cz-grown B-doped (111)Si wafers (10 Ω cm, thickness $d_{Si}=368\pm3$ μm); a few samples were taken from a (100)Si wafer of similar specifications. These wafers were thinned down to a thickness of either 117 ± 16 or 153 ± 19 μm using cupric-ion chem-mechanical polishing, resulting in wafers polished to optical finish on both sides. Cutting with a diamond saw yielded 1×9-mm^2 platelets, with their long edge along the $[11\bar{2}]$ and $[1\bar{1}0]$ crystal axes of the (111) and (001) main-face Si wafer, respectively. The (111)Si experimental configuration is shown in Fig. 1. Before insertion into the preparation chamber the slices were thoroughly cleaned using a standard procedure described elsewhere.[21] The actual mounting of the slices was realized under an aceton (electronic grade) coating of the Si surface in N_2 ambient. Thermal treatments were carried out in a conventional setup consisting of a double-wall fused-silica tube which could be offset from a resistance-heated furnace.[22]

The thermal nitridation treatment generally consisted of three steps. First, the platelets were heated in a flow of 99.9999% pure H_2 (sent through a liquid-N_2 trap) at a temperature T_{H_2} in the range 1000–1150 °C for times t_{H_2} ranging from 15 to 40 min. This high-T treatment in H_2 is a very efficient means for eliminating any native oxide layer (grown on during the mounting of the sample). Omitting this step resulted in the growth of an oxynitride, rather than stoichiometric Si$_3$N$_4$ *(vide infra)*. This was followed by the actual nitridation treatment at the same temperature T_N ($=T_{H_2}$) for times $t_N=103$–209 min in a 40-SCCM (SCCM denotes cubic centimeter per minute at STP) flow of NH_3 (>99.999%). Finally, the NH_3 was switched to a flow of 99.9999% pure N_2 at $T=T_N$ for times 17–98 min, which treatment effectively constitutes a dehydrogenation. The thermal treatment was finished by rolling away the furnace, thus allowing the samples to cool down in N_2 ambient to room temperature (RT) in about 15–20 min. All treatments described were carried out at a pressure $p\approx1.2$–1.3 atm, and the samples were kept in N_2 ambient between ESR measurements.

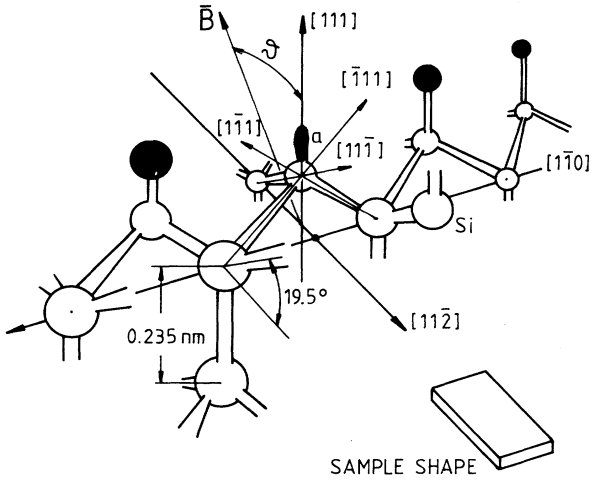

FIG. 1. Schematic view of the atomic configuration at a (111)Si/insulator interface together with applied sample geometry. Entity *a* represents the $sp^3_{[111]}$ Si dangling hybrid.

Two types of samples (A and B) were grown. The thermal treatments for type A, carried out at 1000 °C, consisted of nitridation followed by a nitrogen (dehydrogenation) treatment; no hydrogen pretreatment was applied. Samples B, on the other hand, were subjected to all three treatments (H_2, NH_3, and N_2) at temperatures $T\gtrsim1100$ °C.

B. X-ray photoelectron spectroscopy (XPS)

The stoichiometry and thickness of the (111)Si nitride films were studied by XPS for various values of the exit angle ϑ_i between the photoelectrons and the [111] direction using monochromatized Al $K\alpha_{1,2}$ radiation (energy quantum $E_k=1486.6$ eV). This excitation resulted in an overall resolution for the photoelectron energy of 0.8–0.9 eV, so that the Si 2*p* spin-orbit core-level doublet, which consists of $P_{1/2}$ and $P_{3/2}$ peaks separated by 0.6 eV and with an intensity ratio of 1:2; remained unresolved. The emitted photoelectrons were primarily monitored in the regions around the Si 2*p*, N 1*s*, C 1*s*, and O 1*s* core-level binding energies. Atomic ratios N:Si were calculated using integrated area ratios of the N 1*s* and Si 2*p* peaks, measured with $\vartheta_i=0°$, and previously determined sensitivity factors. During the mounting in the XPS UHV chamber the sample was unavoidably exposed to air ambient, during which time a thin contaminated layer, containing O and C, could form on top of the SiN_x film. The thickness of the superficial layer, however, was much smaller than the effective electron mean free path $\lambda\cos\vartheta_i$ of the N 1*s* and Si 2*p* core electrons, certainly for $\vartheta_i=0°$, so that the overlayer did not impair the probed stoichiometry of the studied Si nitride layers. The SiN_x layer thickness was determined by comparison of its Si 2*p* peaks with those of the Si substrate.

C. ESR spectrometry

Electron-spin resonance (ESR) measurements were carried out using *X*- (8.99 GHz) and *K*- (20.95 GHz) band reflection spectrometers driven in the absorption mode under conditions of slow passage. Narrow-band lock-in detection (sinusoidal magnetic-field modulation at 100–150 kHz) resulted in the detection of absorption-derivative $dP_{\mu a}/dB$ spectra, where $P_{\mu a}$ and **B** represent the absorbed microwave power and applied magnetic field, respectively. Observations were constrained to the region $T\leq40$ K, since at higher T the TE_{011} high-purity copper cavity was excessively loaded due to free-carrier generation in the Si substrate. During the measurements

of the (111)Si samples **B** was rotated either in the $(1\bar{1}0)$ or (111) plane (see Fig. 1), where the direction of **B** in each plane is specified by its angle ϑ with the [111] and $[1\bar{1}0]$ axes, respectively. To increase the signal-to-noise (S/N) ratio, up to 15 platelets were stacked, thus resulting in an effective Si/Si_3N_4 interface of about 3 cm^2 in the cavity. ESR measurements were carried out in the absence of overmodulation, at nonsaturating microwave power (P_μ) levels. For the P_b-type signal observed here at 4.2 K, this requires $P_\mu \leq -16$ dBm for a loaded cavity quality factor $Q \approx 3000$.

Spin concentrations were determined relative to an $Al_2O_3:Cr^{3+}$ susceptibility standard (accuracy $\pm 1\%$) and a secondary Si:P spin standard[23] via double numerical integration of the $dP_{\mu a}/dB$ spectra; relative accuracies obtained are estimated to be $\pm 5\%$. Values of g were determined relative to a LiF:Li g marker[24] of $g_{\mathrm{LiF:Li}} = 2.002\,293 \pm 0.000\,002$.

III. XPS ANALYSIS

A. Influence of the preparation conditions on the chemical properties of the Si-nitride film

XPS spectra ($\vartheta_i = 0°$) of type-A and -B samples are shown in Figs. 2(a) and 2(b), respectively, revealing a distinct difference between both Si nitrides. The Si $2p$ core-level peak centered at the binding energy $E_B^0 = 99.7$ eV originates from Si atoms in the Si^0 oxidation state in the Si substrate, whereas the higher-energy peaks result from the Si^{4+} state in the superficial Si nitride layer. The former peak is detected as the XPS probing depth exceeds the thin (≈ 3 nm) top Si nitride layer and serves as a reference for the chemical shift $\Delta E_B \equiv E_B(Si^{x+}\ 2p) - E_B^0$ of the binding energies E_B (relative to the Fermi level) of other Si $2p$ peaks originating from Si atoms in different oxidation states (Si^{x+}). The obtained Si $2p$ core-level XPS data, together with relevant data from literature, are listed in Table I.

As evidenced in Fig. 2(a), the Si atoms in the grown-on layer of sample A are adequately described by two Gaussian peaks, representing the Si^{4+} and Si^{1+} oxidation states. Comparison of the shift $\Delta E_B = 4.05 \pm 0.1$ eV of the Si^{4+} state with data from literature (see Table I)

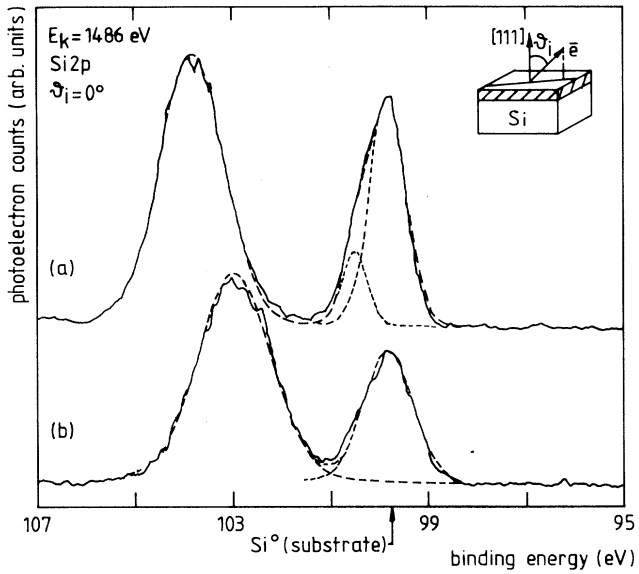

FIG. 2. Si $2p$ core-level XPS spectra ($\vartheta_i = 0°$) excited with Al $K\alpha_{1,2}$ radiation ($E_k = 1486.6$ eV) for sample types A (a) and B (b). The broken curves represent fitted Gauss profiles. The peak at the lower binding energy ($E_B^0 = 99.7$ eV), observed in both spectra, is associated with Si bonded to four Si atoms (Si^0 oxidation state) and serves as a reference for calculating the chemical shifts ΔE_B. The left peak in (a) ($\Delta E_B = 4.05$ eV) corresponds to a Si^{4+} state in an environment of N, O, and Si (oxynitride), while the reference peak itself has admixed a small contribution of Si^{1+} states ($\Delta E_B = 0.70$ eV; cf. small dashed peak) from the top Si nitride layer. The similar peak in (b) ($\Delta E_B = 3.15$ eV), however, corresponds to Si^{4+} in a pure Si_3N_4 environment; no intermediate oxidation states are observed in this case.

shows that it is more typical for the Si^{4+} state in SiO_2 than in Si_3N_4. Calculation of the relative atomic concentrations by comparison of the areas under the N $1s$, O $1s$, and Si $2p$ peaks (the areas under the different peaks were first rescaled using previously determined sensitivity factors) reveals that the type-A toplayer is in fact an oxygen-rich oxynitride film. It is very likely—in view of

TABLE I. Chemical shifts (ΔE_B) and full linewidths at half maximum (FWHM) for the different oxidation states observed in the Si $2p$ core-level spectra shown in Figs. 2(a) and 2(b). The data are compared to values from literature for a-SiO_2 and a-Si_3N_4 films. Comparison of the chemical shifts of the Si^{4+} $2p$ state of spectrum (a) with the data from literature shows a much closer agreement with the a-SiO_2 film than with the a-Si_3N_4 film. The enhanced width of the peaks in spectrum (a) refers to a large-N contamination. Spectrum (b) shows a close resemblance to a-Si_3N_4 as regards both ΔE_B and the FWHM.

Oxidation state	Spectrum (a)		Spectrum (b)		a-SiO_2[a]		a-Si_3N_4[b]	
	ΔE_B (eV)	FWHM (eV)	ΔE_B (eV)	FWHM (eV)	ΔE_B (eV)	FWHM (eV)	ΔE_B (eV)	FWHM (eV)
Si^{1+}	0.7±0.1	0.58±0.05			0.95	0.44[c]	0.78	
Si^{4+}	4.05±0.1	1.58±0.03	3.15±0.1	1.77±0.03	3.9	1.15[c]	3.12	1.9

[a]Reference 26.
[b]Reference 27, values for chemical-vapor-deposited (CVD) material. These data were chosen to compare with, because, like the present films, they were prepared at high T (500–1000°C) too.
[c]The linewidths have been corrected for instrumental broadening.

the very thin Si nitride layer ($\approx$30 Å) ultimately grown—that the growth of an oxynitride rather than a Si_3N_4 film results from admixing of an initial, albeit very thin, native oxide layer.[25] That this has indeed been the case, rather than any O impurification of the ambient gases during thermal cycling, follows from a comparison of the XPS data of sample A with those of type B.

Comparison of the rescaled XPS areas under the N 1*s* and Si 2*p* core-level peaks of sample B convincingly shows that the grown-on films consist of stoichiometric Si_3N_4. This is further corroborated by the agreement (see Table I) of the chemical shift of the Si^{4+} 2*p* level in spectrum (b) with that of Si_3N_4 (literature), for which reason we will henceforth refer to type-B films as Si_3N_4 layers. The result demonstrates the efficiency, as expected, of a short high-T H_2 pretreatment prior to thermal nitridation in NH_3, in removing any remaining (native) oxide from the Si substrate. This is in line with previous Auger electron spectroscopy data[4] for nitride films grown in 100% ammonia.

A more detailed XPS analysis of the Si_3N_4 films (samples B) shows that the Si^{4+} 2*p* core-level peak width is substantially lower than reported in literature (Table I). While this may partly be due to the resolution inherent in the XPS spectrometer, it also reflects the local homogeneity of the film; the reduced width has likely resulted from the growth at higher $T(>1100\,°C)$ of the thermal a-Si_3N_4 as compared to the lower deposition temperature (500–1000 °C) of chemical vapor deposition (CVD) material, and the high-T post-nitridation annealing (PNA) in N_2. In this way, the lower incorporation of hydrogen is further reduced by the PNA—the PNA will break or remove remaining SiH_x and NH_x species[28]—leaving a nitride film primarily consisting of SiN_4 tetrahedra. It follows that there is almost no distribution in local charge transfer as a result of a distribution in the chemical nature of the nearest and second-nearest neighbors of a Si atom.

A next aspect regards the chemical homogeneity of the Si nitride film versus depth. Since no secondary Si 2*p* peaks nor even shoulder peaks (asymmetry) are detected [Fig. 2(b)], any segregation or inhomogeneities in the present Si_3N_4 films appear absent. Moreover, with no hydrogen incorporated, small linewidths for a-Si_3N_4 can be expected as the bond angle distributions are very narrow for both Si and N. This has been evidenced in previous XPS work on deposited SiN_x as well.[29] A study of the ratios of the N 1*s*, O 1*s*, C 1*s*, and Si 2*p* peaks as a function of the take-off angle ϑ_i shows the majority of the nitride film to consist of stoichiometric Si_3N_4. Only a few superficial monolayers on top of the nitride film appear contaminated with O and C, as born out by the strongly increasing O 1*s* and C 1*s* peaks for large exit angle.[30] This contamination has obviously resulted from exposing the films to air ambient after fabrication. However, measurements of the Si 2*p* core-level spectra at different exit angles ($\vartheta_i = 0°$, 60°, and 80°) show almost no change in ΔE_B and linewidth, as is clear from the inset in Fig. 3. This again proves the homogeneity of the greater part of the film as a function of the sampled film depth.

No oxidation states of Si other than Si^{4+} can be distinguished in the Si_3N_4 spectrum (b) of Fig. 2. Taking into account the thickness of the film ($\approx$30 Å), as estimated from XPS data below, this means that the existence of Si atoms in other oxidation states near the interface must be limited to a few monolayers at most so as to be unobservable by XPS. This suggests that the sharpness of the thermally grown Si_3N_4/(111)Si interface approaches that of thermal SiO_2/(111)Si.

B. Measurement of the film thickness

Measurement of the film thickness by XPS requires the knowledge of a few photoelectron properties as well as material-related parameters, which will be introduced below. These parameters are sometimes available in literature. If not, they have to be determined by XPS measurements on a reference sample of well-known composition, of which the thickness is obtained by an in-

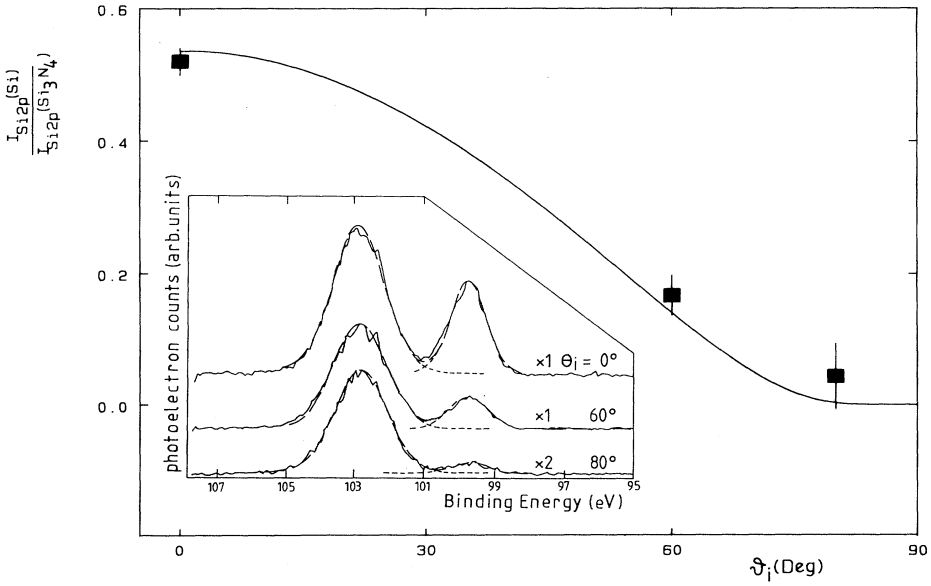

FIG. 3. Intensity ratio of the Si^{0+} 2*p* and the Si^{4+} 2*p* peaks vs the photoelectron takeoff angle ϑ_i for a stoichiometric Si_3N_4/(111)Si sample (type B). The data are obtained from XPS spectra shown in the inset, where the broken curves are fitted Gauss profiles. The constant linewidth of the Si^{4+} peak in the XPS spectra as a function of ϑ_i is indicative of the homogeneity and purity of the Si_3N_4 film (no oxygen contamination). The solid line through the data is the fit obtained from Eq. (2), giving a Si_3N_4 film thickness of 31±3 Å.

dependent technique (e.g., ellipsometry or a stylus profilometry). Lack of a reference sample and data in literature for oxynitrides (samples A)—one can even question whether it is possible to grow a reference oxynitride at all in light of the innumerable number of oxynitride varieties one may obtain—limited the thickness measurements to stoichiometric Si_3N_4 films (samples B).

The Si_3N_4 film thickness was determined by comparison of the area $I_{Si\,2p}(Si_3N_4)$ under the Si^{4+} $2p$ core-level peak of Si atoms in Si_3N_4 with the area $I_{Si\,2p}(Si)$ under the substrate Si^0 $2p$ peak. The intensity $I_{Si\,2p}(Si_3N_4)$ for the Si_3N_4 overlayer of thickness d is obtained by integrating over the exponential escape probability[31,32]

$$I_{Si\,2p}(Si_3N_4)=K_{Si\,2p}(Si_3N_4)\sigma_{Si\,2p}(Si_3N_4)\rho_{Si}(Si_3N_4)\times\int_0^d \exp\left[\frac{-z}{\lambda_{Si\,2p}(Si_3N_4)\cos\vartheta_i}\right]dz\ . \quad (1)$$

In this expression, $K_{Si\,2p}(Si_3N_4)$ represents the spectrometer constant for measuring Si $2p$ photoelectrons originating from Si_3N_4 (incorporating factors such as x-ray flux, fraction of photoelectrons collected, geometrical factors, counting efficiency, etc.), $\rho_{Si}(Si_3N_4)$ is the partial density (g/cm^3) of Si atoms in the Si_3N_4 film, $\lambda_{Si\,2p}(Si_3N_4)$ is the mean electron escape depth of Si^{4+} $2p$ electrons in the Si_3N_4 film, and $\sigma_{Si\,2p}(Si_3N_4)$ is the corresponding electric photoionization cross section. The intensity from the underlying Si substrate is given by a similar expression, except that it is additionally multiplied by the attenuation factor $\exp[-d/(\lambda_{Si\,2p}(Si_3N_4)\cos\vartheta_i)]$ of the Si_3N_4 film. Combining this with Eq. (1), and assuming that the $K_{Si\,2p}$ and $\sigma_{Si\,2p}$ values of the Si substrate and Si_3N_4 film are equal (the latter is a good approximation as $|\Delta E_B| \ll E_B$ and $E_B \ll E_k$) leads to the intensity ratio

$$\frac{I_{Si\,2p}(Si_3N_4)}{I_{Si\,2p}(Si)}=\frac{\rho_{Si}(Si_3N_4)}{\rho_{Si}(Si)}\frac{\lambda_{Si\,2p}(Si_3N_4)}{\lambda_{Si\,2p}(Si)}\left[\exp\left[\frac{d}{\lambda_{Si\,2p}(Si_3N_4)\cos\vartheta_i}\right]-1\right]. \quad (2)$$

Using the densities $\rho_{Si}=2.33$ g/cm^3 and $\rho_{Si_3N_4}=3.44$ g/cm^3,[33] gives $\rho_{Si}(Si)=\rho_{Si}=2.33$ g/cm^3 and $\rho_{Si}(Si_3N_4)=(84/140)\rho_{Si_3N_4}=2.07$ g/cm^3. The inelastic mean free path λ may be obtained from the semiempirical formula[34]

$$\lambda=\frac{538}{(E_k)^2}a_A+0.41a_A(a_AE_k)^{1/2}\ , \quad (3)$$

where E_k is in Ev and a_A is the mean atomic radius in nm. However, as the standard deviation on λ, as calculated from Eq. (3), turns out to be rather large, it is preferable to use experimentally obtained values for λ. It is generally accepted that $\lambda_{Si\,2p}(Si_3N_4)=30$ Å (Ref. 35) for stoichiometric Si_3N_4 when applying Al $K\alpha_{1,2}$ x-ray excitation, while the value $\lambda_{Si\,2p}(Si)=26$ Å is obtained experimentally[36] for the Si^0 $2p$ core level in a Si crystal. Substitution of all values in Eq. (2) leaves the thickness d as the only unknown parameter. Fitting of Eq. (2) to the $I_{Si\,2p}(Si)/I_{Si\,2p}(Si_3N_4)$ data obtained for various exit angles. ϑ_i (cf. Fig. 3) results in a thickness $d=31\pm3$ Å for the Si_3N_4 film (sample B), which is in good agreement with other data[4,37] on thermally grown pure Si_3N_4 films. The thermal nitride and oxynitride films are expected to be of equal thickness.

IV. EXPERIMENTAL ESR RESULTS

Initial ESR measurements were carried out in Si/Si nitride structures not subjected to a post-nitridation N_2 anneal. However, no signal could be observed. This could mean either that the samples did not contain any (ESR active) defects or that the defects were left passivated by H (Ref. 22) after the NH_3 treatment. The latter appeared to be the case, as became evident after applying a post-nitridation N_2 anneal. In Fig. 4 are shown characteristic X- and K-band ESR spectra observed for $\mathbf{B}\|[11\bar{2}]$ and $T=4.2$ K, of (111)Si/Si_3N_4 samples of type B, subjected to a final high-T dehydrogenation in N_2 ambient. Three signals are observed: number III is the Si:P marker signal, while the other signals (I and II) pertain to the (111)Si/Si nitride structure.

A. K center

Signal II, with $g=2.0028\pm0.0001$, is observed in stoichiometric Si_3N_4 films (Fig. 4) only; it behaves fully isotropically and exhibits a linewidth which scales linearly with the microwave frequency (an indication for a g tensor powder pattern as is observed for defects in amor-

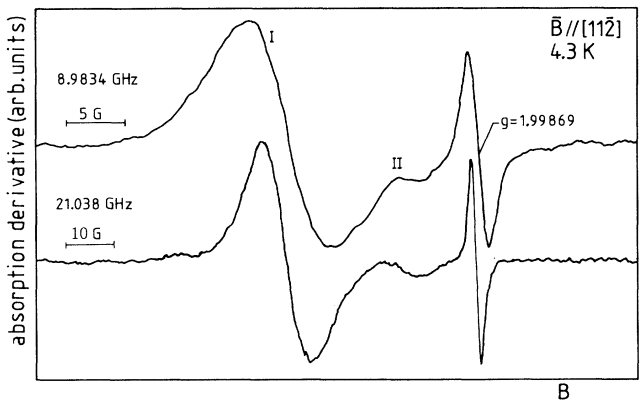

FIG. 4. X- and K-band ESR spectra observed at 4.3 K using $P_\mu=-16$ dBm on a (111)Si/Si_3N_4 (type B) sample, grown by thermal nitridation in NH_3 (preceded by an *in situ* native oxide removal) for 123 min at 1000±20 °C followed by an anneal in N_2 for 24 min at the same T. The signal at $g=1.998\,69$ originates from a Si:P reference signal. Signals I and II are ascribed to Si sp^3 hybrid dangling bonds at the (111)Si/insulator interface ($\cdot Si \equiv Si_3$) and in bulk Si_3N_4 ($\cdot Si \equiv N_3$), respectively.

phous solids) giving ΔB_{pp} (X band)= 2.4±0.3 G and ΔB_{pp} (K band)= 6.3±0.8 G. A signal with the same signature has frequently been reported in silicon nitrides prepared in various ways, though with some spread in g and ΔB_{pp}.[38,39] It has been ascribed to a dangling bond (DB) on a Si atom, backbonded to three N atoms (·Si≡N$_3$). The Si dangling-bond nature is in good agreement with the easy H passivation and dehydrogenation disposed by the defect (see, e.g., Ref. 22). Depending on the detailed preparation conditions applied, it has been shown[9,39,40] that the Si dangling-bond g value can continuously be shifted from $g=2.0055$ (·Si≡Si$_3$) in a-Si to $g=2.0028$ (·Si≡N$_3$) in stoichiometric a-Si$_3$N$_4$. The lowering of the defect's g value with increasing number of N ligands was theoretically predicted.[4] So the measured g value of signal II refers not only to the DB-like nature of the defect, but also provides additional evidence for the stoichiometric nature of the nitrides presently studied. The observation that the linewidth is somewhat smaller than usually observed in stoichiometric CVD nitride films ($\Delta B_{pp}\approx 12$ G) (Refs. 39 and 40) is ascribed to improved chemical homogeneity (high purity and low hydrogen content) and reduced local bond angle distortion (structural homogeneity) of the present Si nitride films as compared to low-T CVD material. This is confirmed by the XPS measurements. The measured signal-II concentration of $\approx 2.3\times 10^{17}$ cm^{-3} is also typical for stoichiometric a-Si$_3$N$_4$ films.[28]

The appearance of a similar line in the range $g=2.003-2.005$ might be expected in the oxynitride films. No such signal, however, has been detected, likely due to the far greater chemical and structural disorder in the oxynitride films as compared to the stoichiometric nitrides. Indeed, it was shown by XPS that the Si 2p linewidth in (oxy)nitrides increases significantly[29,40] when the preparation conditions are tuned away from those leading to stoichiometric nitrides. This results from the high sensitivity of the Si 2p chemical shift to changes in the chemical nature of the ligands and the related bond angles. The chemical nature of the ligands in stoichiometric nitrides is set by nitrogen only and, occasionally, H—in our high-T samples the hydrogen concentration is low. In oxynitrides, however, there may be a great variety in the overall chemical nature of the ligands (O, N, and H) surrounding a Si atom. The resulting greater inhomogeneity of the chemical shift accounts for the greater Si 2p XPS linewidth. Similar to the chemical shift in XPS, the $\tilde{g}$ dyadic of a Si dangling-bond defect is also quite sensitive to small changes in the positions and chemical nature of the ligands—this is especially true for $g_\perp$,[42] the g value for $\mathbf{B}\in(111)$—so the resulting ESR signal (II) will reflect a large distribution of g values in the range $g=2.003-2.005$. The ensuing excessive broadening has likely prevented the detection of the signal.

B. ·Si≡Si$_3$ interface defect; P_{bN}

Signal I is observed in both types of samples. It is ascribed to electrons in singly occupied Si dangling-bond orbitals, pointing into the [111] direction (perpendicular to the interface) and located at the (111)Si/Si nitride interface. This identification stems from the various striking similarities with the similar [111]P_b defect at the (111)Si/SiO$_2$ interface. First, the signal is well in registry with the Si substrate lattice and exhibits axial (C_{3v}) symmetry around the [111] axis. The g tensor data for $\mathbf{B}\in(1\bar{1}0)$, illustrated in Fig. 5 for both samples A and B, come out quite similar, although the g anisotropy of the (111)Si/oxynitride structure (sample A) appears somewhat larger. The fact that only one limb of the g map is observed is in favor of the defect's localization at the interface, rather than being a bulk Si defect. Second, the principal g values, obtained by fitting

$$g(\vartheta)=[(g_\parallel\cos\vartheta)^2+(g_\perp\sin\vartheta)^2]^{1/2} \tag{4}$$

to the data in Fig. 5 (dotted line), strongly support the defect's dangling-bond-like character, i.e., $g_\parallel=2.001\,49\pm 0.000\,03\approx g_0$ and $g_\perp=2.008\,52\pm 0.000\,07>g_0$.[13,42] These g values were confirmed by measurements on the (001)Si/(oxy)nitride interface. At the latter interface, however, the various variants, i.e., with the unpaired sp^3 hybrid pointing along [111], [11$\bar{1}$], [1$\bar{1}$1], or [$\bar{1}$11], are observed in equal intensities. This leads to overlapping resonances such that this interface was not well suited for detailed investigation. This is in contrast with the (111)Si/(oxy)nitride interface where the unpaired $sp^3_{[111]}$ variant is dominant. Third, alternation of chemical etch-back experiments in diluted HF (5 vol %) with ESR defect concentration measurements revealed the interfacial

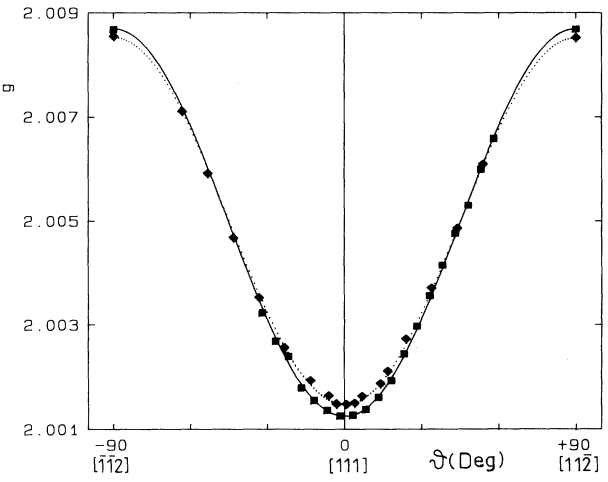

FIG. 5. g map of the P_{bN} center at the (111)Si/oxynitride (type A: ■) and the (111)Si/Si$_3$N$_4$ interface (type B: ◆) for $\mathbf{B}\in(1\bar{1}0)$; ϑ is the angle between $\mathbf{B}$ and [111]. The solid (sample A) and dotted curves (sample B) are obtained by fitting Eq. (4), giving the principal g values $g_\parallel=2.001\,25\pm 0.000\,03$, $g_\perp=2.008\,69\pm 0.000\,04$ and $g_\parallel=2.001\,49\pm 0.000\,03$, $g_\perp=2.008\,52\pm 0.000\,07$, respectively. The ESR settings are a microwave frequency of 21.038 GHz, $P_\mu=-16$ dBm, and $T=4.3$ K. Sample B is the same as described in Fig. 4. Sample A was thermally nitrided in NH$_3$ for 209 min at 1000 °C followed by an anneal in N$_2$ for 28 min at the same temperature.

location of defect I, in contrast with defect II, that was found to reside in the Si_3N_4 film. Fourth, the areal density (N_S) of signal-I centers varies in the range $(7-32)\times10^{12}$ cm^{-2}. These values are somewhat larger than the typical P_b densities observed in as-grown conventional thermal (111)Si/SiO_2, i.e., $N_S\approx(4-5)\times10^{12}$ cm^{-2}. However, as shown below, this is partly a consequence of dehydrogenation during the N_2 anneal. In effect, one should compare the defect-I densities with the P_b concentration[43] $[P_b]=(11.6\pm1.1)\times10^{12}$ cm^{-2} of a fully dehydrogenated (111)Si/SiO_2 interface grown at $T=950$ °C. The larger rigidity of the Si nitride may necessitate that many more dangling bonds be generated at the interface to relieve the enhanced interface stress.[44] It should be noted, though, that the maximum N_S value is still much less than the number of Si atoms (N_a) in one (111)Si plane, i.e., $N_a=7.830\times10^{14}$ cm^{-2}, as expected. It needs to be remarked that, irrespective of the greater radiation hardness of (oxy)nitrides,[3] the high intrinsic concentration (passivated by H or not) of P_b-like defects at the (111)Si/(oxy)nitride interface may lead to serious degradation in the long run (instabilities) when these interfaces are applied in MISFET (metal-insulator-semiconductor field-effect transistor) technology,[45] especially when used in harsh radiation environments. Fifth, conclusive evidence finally comes from the observation of the primary ^{29}Si hf signals of defect I for a type-B sample at $T=4.2$ K. The ratio of the areas under the central line and the hyperfine signals is consistent with the localization of the unpaired defect electron on mainly *one* Si atom, i.e., the "apex" Si atom, taking into account a natural ^{29}Si (nuclear spin $I=\frac{1}{2}$) abundance of 4.70%. The observed hf splitting $A_{\parallel}(\mathbf{B}\parallel[111])=156\pm4$ G equals the one observed for the P_b defect at the (111)Si/SiO_2 interface,[14] referring to a similar hybridization of the molecular orbital. This shows that the primary properties of the Si dangling-bond wave function are determined by the backbonded Si matrix and not by the overlaying insulator. The width of the hf signals $\Delta B_{pp}=18\pm1$ G, is somewhat broader than the value $\Delta B_{pp}=15\pm1$ G observed on standard Si/SiO_2 interfaces.[14]

The close similarity of the salient ESR features indicates the basic structure of defect I and the P_b defect at the thermal Si/SiO_2 interface to be identical. Therefore, we will henceforth label defect I as $[111]P_{bN}$ (Ref. 20)—or simply as P_{bN} if no confusion can occur—in analogy with the $[111]P_b$ defect in thermal (111)Si/SiO_2.

But while the primary ESR signatures are similar, there are secondary, though significant, differences as well. Indeed, it cannot be expected that the natural interfaces *c*-Si forms with two dissimilar solids (Si compounds) are identical in every respect. This not only applies for P_b and P_{bN} defects, but is even observed when comparing P_{bN} defects in samples A and B. These dissimilarities merit further analysis because they may shed new light on the impact of the insulator capping the $P_b(P_{bN})$ defect. Their systematic exploration is, therefore, a primary goal of the present study.

A first noteworthy dissimilarity between the thermal (111)Si/(oxy)nitride and the (111)Si/SiO_2 interfaces is the saturating microwave power. For high-quality thermal Si/SiO_2, the P_b spin temperature already starts to rise for $P_\mu\approx-63$ dBm and $Q\approx13\,000$ at $T=4.2$ K and the *K*-band frequency.[22] The extreme saturatibility of some Si/SiO_2 structures may in fact prevent undistorted measurements at liquid-He temperatures.[46] In the case of the (oxy)nitrides, saturation effects become observable at $P_\mu\approx-19$ dBm for $Q\approx3000$. Despite the difference in Q, this discrepancy is remarkably large, the reason for which must be found in the fundamentally different ways the respective spin systems relax magnetic energy to the lattice. It is interesting to note, however, that the saturation behavior of the P_b system at the *native oxide/* (111) Si interface[18] very much resembles that of the P_{bN} defects at the (111)Si/(oxy)nitride surface.

In Fig. 6 is illustrated the ESR linewidth anisotropy for type-A and -B samples, together with data for thermal (111)Si/SiO_2 for $T=4.2$ K and $\mathbf{B}\in(1\bar{1}0)$. For this comparison, a dehydrogenated Si/SiO_2 structure has been chosen with a (ESR active) concentration $[P_b]\approx(12.8\pm1)\times10^{12}$ cm^{-2}, which is of the same magnitude as $[P_{bN}]$ in samples A and B. Filled and open symbols refer to *K*- and *X*-band data, respectively. Typical P_b linewidths in as-grown conventional (111)Si/SiO_2 range from 1.3 to 1.5 G for $\mathbf{B}\parallel[111]$. For the highest concentration, ΔB_{pp} can increase to 1.90 ± 0.02 G due to dipolar broadening,[22] as is the case in Fig. 6. These data actually are those of sample *S*1 in Ref. 22. The same linewidth ($\mathbf{B}\parallel[111]$) is observed at the *X* band, showing there is little influence of frequency-dependent broadening for $\mathbf{B}\parallel[111]$. For $\mathbf{B}\parallel[11\bar{2}]$, however, the P_b linewidths increase to 6.3 ± 0.1 and 3.4 ± 0.1 G at the *K* and *X* bands,

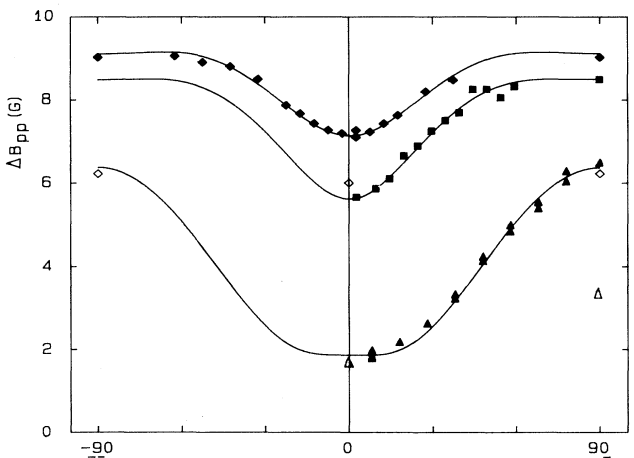

FIG. 6. Linewidth anisotropy of the interfacial $\cdot Si\equiv Si_3$ defect observed at $T=4.3$ K and $\mathbf{B}\in(1\bar{1}0)$ for three interfaces: (111)Si/SiO_2 (▲), (111)Si/oxynitride (■), and (111)Si/Si_3N_4 (◆). Open and solid symbols represent *X*- and *K*-band data, respectively. The thermal oxide (920±15 °C; 63 min; 150-Torr O_2) was grown to a thickness of 134±5 Å and subsequently dehydrogenated at ~835 °C in vacuum ($p\lesssim2\times10^{-5}$ Torr). The oxynitride and nitride were thermally grown in NH_3 at 1000±20 °C for 209 min and at 1120±20 °C for 206 min, respectively.

respectively, revealing a significant frequency-dependent ($\overleftrightarrow{g}$ dyadic) broadening.[13,47] In the case of interfaces A and B, typical linewidths for $\mathbf{B}\|[111]$ at the K band are 5.6 and 7.1 G, respectively, while the X-band linewidth $\Delta B_{pp}(X)$ for sample B decreases to 6.0±0.3 G. For $\mathbf{B}\|[11\bar{2}]$, the K-band P_{bN} linewidths are 8.5±0.1 and 9.0±0.1 G for sample types A and B respectively, while the X-band-width for sample B decreases to 6.2±0.3 G. Comparison of these ΔB_{pp} data reveals three major differences. First, the observed dangling-bond linewidth clearly depends on the nature of the top insulator. The by far smallest values are obtained for the P_b defect in thermal Si/SiO$_2$, followed by the P_{bN} linewidth in Si/oxynitride, the largest pertaining to the P_{bN} defect at the (111)Si/stoichiometric nitride interface. Along one interpretation, this may refer to a dependence of ΔB_{pp} on the *chemical* nature of the $P_b(P_{bN})$'s neighbors (unresolved hf interactions). Second, the X- and K-band data coincide for $\mathbf{B}\|[111]$ only for P_b at the (111)Si/SiO$_2$ interface; at the (111)Si/(oxy)nitride interfaces, by contrast, there is a substantial frequency-dependent contribution in ΔB_{pp} for all $\mathbf{B}$ orientations. In the molecular-orbital representation of the dangling-bond orbital, no influence of the interface strain on the linewidth is expected to first order for $\mathbf{B}\|[111]$.[13] We may therefore anticipate either a fundamentally different behavior of the interface strain at the (oxy)nitride interface as compared to the Si/SiO$_2$ interface or a modification of the P_{bN} wave function as compared to the P_b one. Third, as illustrated in Fig. 6, the linewidth anisotropy of the P_{bN} defect is distorted, i.e., is substantially smaller than the P_b one. The broadening of the P_{bN} width with increasing ϑ already flattens out at $\vartheta \approx 60°$, in contrast to the P_b behavior.

The P_{bN} linewidth shows a distinct T dependence, as illustrated in Fig. 7 for sample B in the range $4.2 < T \lesssim 40$ K. X- and K-band linewidths are plotted for both the $\mathbf{B}\|[111]$ and $\mathbf{B}\|[11\bar{2}]$ directions. A profound narrowing of ΔB_{pp} with increasing T is observed for both directions and microwave frequencies, the decline being steepest for $\mathbf{B}\|[111]$. It is interesting to note, again, that a similar behavior was previously observed for P_b defects at nonstandard Si/SiO$_2$ interfaces[47]—not so, by contrast, for P_b at the standard thermal (111)Si/SiO$_2$ interface. It is also clear from Figs. 6 and 7 that at $T=4.2$ K and for $\mathbf{B}\|[111]$, the X- and K-band linewidths do not coincide. Both linewidths, however, become increasingly closer as $T \to 40$ K, tending to coincide, presumably, at somewhat higher T for $\mathbf{B}\|[111]$. In contrast, this appears less obvious for the X- and K-band linewidths for $\mathbf{B}\|[11\bar{2}]$.

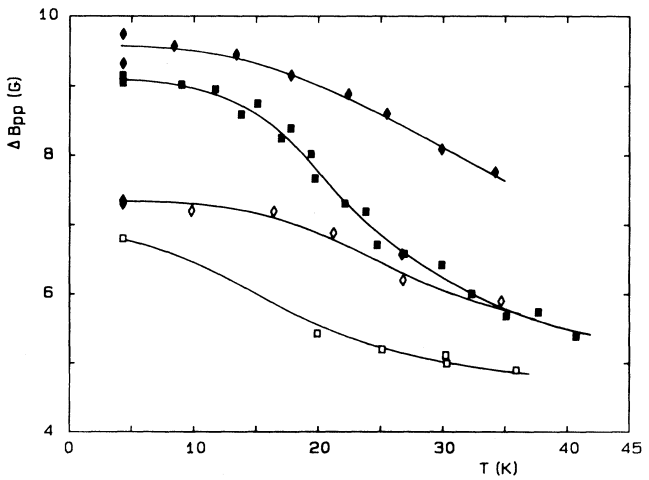

FIG. 7. T dependence of the absorption-derivative linewidth of a (111)Si/Si$_3$N$_4$ sample for $\mathbf{B}\|[111]$ (□) and $\mathbf{B}\|[11\bar{2}]$ (◇). Open and solid symbols represent X- and K-band data, respectively. The sample studied is the same as in Fig. 4. Curves are meant to guide the eye.

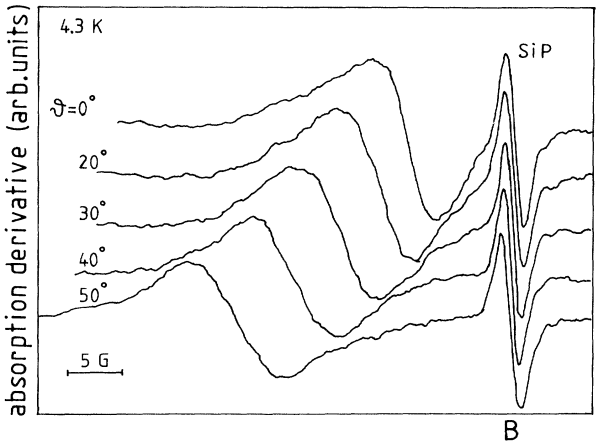

FIG. 8. K-band ESR line shapes [$\mathbf{B} \in (1\bar{1}0)$] of P_{bN} defects at the (111)Si/Si$_3$N$_4$ interface for different values of ϑ.

The 4.2-K P_{bN} resonance for sample B is illustrated in Fig. 8 for different values of ϑ. Beside the varying linewidth as a function of ϑ, asymmetric features in the line shape are evident. The width is smallest for $\vartheta=0°$, where the resonance shape exhibits a low-field wing much broader than the high-field one. When $\vartheta \to 60°$, the line broadens significantly while the asymmetry fades away, the shape being almost symmetric for $20 < \vartheta < 70°$. For ϑ beyond 60°, the linewidth almost stagnates but a reversed asymmetry develops, now with a long tail on the high-field side. This asymmetry is maximal for $\vartheta=90°$ ($\mathbf{B}\|[11\bar{2}]$). While the reversal and loss of the asymmetric shape may appear rather unusual, it was, nevertheless, duplicated in numerous samples (types A and B).

An interesting related observation is that, along with the line narrowing, the line shape asymmetry gradually fades with increasing T. At $T \approx 30$ K, the asymmetry has disappeared and the linewidth anisotropy has now evolved to the one typical for P_b at the (111)Si/SiO$_2$ interface (see Fig. 6). At this temperature, the line shape is almost Lorentzian for $\vartheta=0°$, tending to a more Gaussian character with increasing ϑ so as to become nearly perfectly Gaussian for $\vartheta=90°$; the X- and K-band linewidths are identical for $\mathbf{B}\|[111]$, which is also in line with the P_b

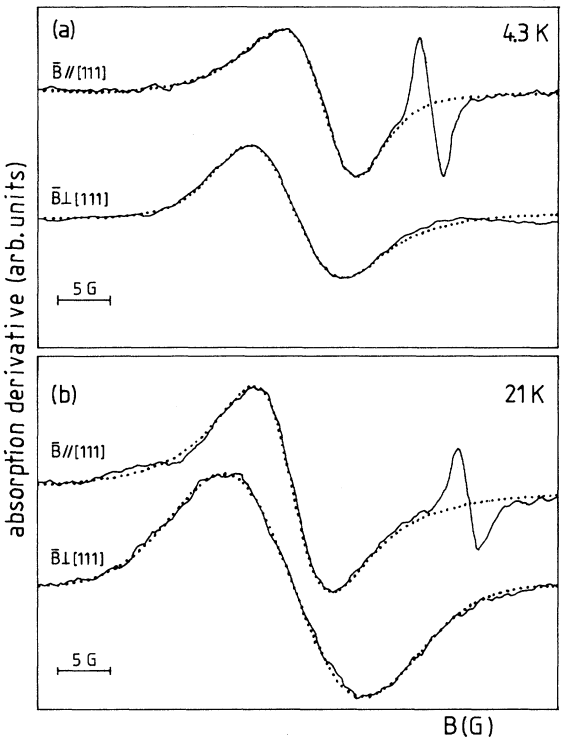

FIG. 9. K-band P_{bN} line shapes for a (111)Si/Si_3N_4 sample observed with $\mathbf{B}\|[111]$ ($\vartheta=0°$) and $\mathbf{B}[11\bar{2}]$ ($\vartheta=90°$) at 4.3 (a) and 21 K (b), respectively. The dots represent fits using the model outlined in Sec. V B. The sample studied is the same as in Fig. 6.

behavior.[13,47] Typical high-T P_{bN} spectra are shown in Fig. 9(b).

V. INTERPRETATION AND DISCUSSION

It has been shown that, despite salient similarities, there also exist differences in the ESR characteristics of the various interfacial $\cdot Si\equiv Si_3$ centers depending on the nature of the top insulator, such as regarding the linewidth, line shape, and T dependence. To deal with this, here we will outline a general model of the interfacial trivalent Si defect center suited for the various interfaces (Si/thermal oxide, native oxide, oxynitride, and stoichiometric nitride). In a second step, the model will be tested experimentally for the (111)Si/Si_3N_4 interface. For clarity, we will restrict the discussion to the (111) interface.

A. $P_{b(N)}$ model

The essence of the P_b model, as illustrated in Fig. 1 for the (111)Si/SiO_2 interface, has been extensively described previously.[12–14,22] P_b's paramagnetism arises from an unpaired electron predominantly localized within a $sp^3_{[111]}$ hybrid (perpendicular to the interface) on a threefold-coordinated substitutional Si atom at the interface. Using molecular-orbital theory the projection of the P_b defect wave function Ψ_{DB} on the $3s$ and $3p_{[111]}$ atomic orbitals of the central Si atom is represented by

$$\Psi_{DB}=\eta(\alpha|3s\rangle+\beta|3p_{[111]}\rangle)\ , \tag{5}$$

with $\alpha^2+\beta^2=1$. Here η^2 is the localization parameter on the central Si atom, and α^2 and β^2 are the amount of s and p character in the dangling bond. The observation of the ^{29}Si hf interaction showed that $\eta^2=0.80$, $\alpha^2=0.12$, and $\beta^2=0.88$.[14,48–50] This indicates that 80% of the spin density[51] is localized on the central interfacial Si atom and that the hybrid orbital is 12% s like and 88% p like. These experimental facts were corroborated later on by elaborate molecular-orbital-type calculations[52,53] on extended clusters, that took into account spin polarization effects, thus providing improved wave-function parameters at the P_b site. The P_b center has C_{3v} symmetry within the accuracy of the ESR measurements. The sharpness and lack of any apparent splitting in the resonance line for $\mathbf{B}\|[111]$ means that, in the case of conventional (111)Si/SiO_2, the dangling bond is essentially perpendicular to the interface[13] (see Fig. 1); it does not reflect any surface irregularities such as adjacent ledges or atomic steps as part of the immediate structure of the P_b center.[13,22]

Interface strain does have an influence on the P_b spectrum, resulting in an anisotropy of the linewidth and line shape:[44] The reason for this traces back to the atomic origin of the g anisotropy for dangling bonds.[13,42] Using molecular-orbital theory the anisotropy in the $\overleftrightarrow{g}$ dyadic for a sp^3 hybrid orbital is calculated to be axial around the dangling-bond symmetry axis with

$$g_{\|}(\mathbf{B}\|[111])=g_0 \tag{6}$$

and

$$g_{\perp}(\mathbf{B}\perp[111])=g_0+\Delta g_{\perp}\ , \tag{7}$$

where

$$\Delta g_{\perp}=\lambda_{3p}\left[\frac{1+\epsilon}{E_b}-\frac{1-\epsilon}{E_a}\right]\beta^2\ . \tag{8}$$

In this expression, λ_{3p} is the spin-orbit constant for the $3p$ atomic wave function, E_a and E_b are the defect's antibonding and bonding energy levels, and $\epsilon\sim0.17$ is a scale factor for the overlap between the valence and core wave function.[42] The direct consequence of the dependence of $g_{\perp}$ on β^2 is that slight variations in bond length and angles in the neighborhood of the P_b defects due to interface strain may produce a variation in the defect's hybridization ratio β^2/α^2 and, *a fortiori*, a distribution $\delta g_{\perp}$ in $g_{\perp}$. This distribution is manifested by growing broadening of the P_b signal when $\mathbf{B}$ is tilted away from the [111] axis: indeed, the influence of $g_{\perp}$ on g (and thus on the resonance field) grows when ϑ increases [cf. Eq. (4)]. When $\mathbf{B}\|[111]$ this broadening of the P_b resonance vanishes for a completely axially symmetric dangling bond ($g=g_0$), and the linewidth is then mainly determined by the envelope of the unresolved ^{29}Si hyperfine interactions at low concentrations. The attendant natural (constituent) line shape is Voigt-like, as observed on high T_{ox} ($T_{ox}\gtrsim850\,°C$) standard (111)Si/SiO_2.[13,22] At higher

P_b concentrations [P_b] the line shape evolves to Lorentzian as it is increasingly more dominated by dipole-dipole interactions within the two-dimensional P_b spin system.[22]

This P_b model for thermal (111)Si/SiO$_2$ can be generalized for the P_{bN} defect at the (111)Si/(oxy)nitride interface, though with some added extensions or modifications reflecting inherent differences in the top layers. First, due to unequal natural abundances ζ_n of nuclear spin, the P_{bN}'s linewidth and shape may be more affected by hf interaction with nearby N atoms [nuclear spin $I(^{14}\mathrm{N})=1$; $\zeta_n=99.63\%$] in the top Si nitride layer than P_b by overlapping O atoms [$I(^{17}\mathrm{O})=\frac{5}{2}$; $\zeta_n=0.037\%$]. Second, as a result of the increased interface strain—(oxy)nitride layers are far more rigid than SiO$_2$ films—the cylindrical symmetry of the P_{bN} defect is not necessarily retained. For simplicity, we will describe this perturbation of the symmetry as a lateral relaxation, i.e., a relaxation of only the central Si atom away from its axial position relative to the three backbonded Si atoms in the substrate—it may be roughly pictured as a tilting of the unpaired sp^3 hybrid. This symmetry distortion gives rise to a second, though specific, distribution of g in addition to the above-mentioned distribution (in $g_\perp$) resulting from symmetry-preserving variations in bond length and angles [e.g., a *vertical* ($\|[111]$) movement of the central Si atom].[54] In reality, of course, the perturbation of the symmetry will be a consequence of the distortion of the bond angles and bond lengths not only as a result of the displacement of the central Si atom but also of its immediate neighbors. However, the displacement of only the central Si atom will be a good first approximation because of the greater positional rigidity of the substrate Si atoms. The relaxation and attendant lowering of the energy may proceed in different directions. As a result, the C_{3v} symmetric ground state is replaced by a set of (nearly) degenerate energy levels, which correspond to the (slightly) different distorted configurations to which the P_{bN} defect may relax. The lowering of the energy by relaxation to additional P_{bN} configurations depends on the local interface strain, and, hence, will vary over the interface plane. Third, the (near) degeneracy of the energy levels, corresponding to the different configurations, may lead to a thermally activated dynamic behavior of the defect at higher temperatures. We will show that this model may account for the P_{bN} ESR characteristics.

B. P_{bN}'s line shape and linewidth

Let us now verify whether the proposed refinements may account for the observed linewidth and shape anisotropy of P_{bN} at $T=4.2$ K. We note that, owing to the lowering of the defect's C_{3v} symmetry, the P_{bN} $\overleftrightarrow{g}$ dyadic will no longer be perfectly axially symmetric, nor will the predictions of Eqs. (7) and (8) strictly hold. Although the allowed structural distortions of the P_{bN} center have not been rigorously defined so as to enable a theoretical estimation of the ensuing change in $\overleftrightarrow{g}$, it may be assumed that these are small. This gives a way to the introduction of some simplifications to allow approximate calculations of the linewidth and shape: In a first approximation, the

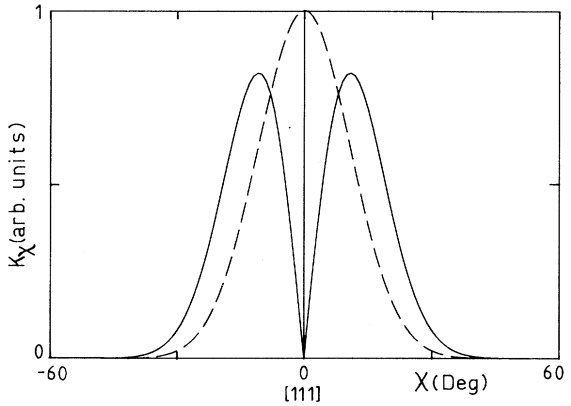

FIG. 10. The effective P_{bN} angular dangling-bond distribution $K_\chi(\chi)$ (solid line) for **B** perpendicular to the (111)Si/Si$_3$N$_4$ interface as obtained from linewidth anisotropy calculations (see Table III). The dashed line is the distribution in one plane, without added solid angle effect.

P_b model at the (111)Si/SiO$_2$ interface, as summarized above, will be retained. This means, first of all, that $\overleftrightarrow{g}$ is axially symmetric with the symmetry axis perpendicular to the interface and, second, that $g_\parallel$ is constant over all P_b sites while $g_\perp$ is described by a *Gaussian distribution* of standard deviation $\delta g_\perp$ (due to interface strain) around the mean $\bar{g}_\perp$. Then, to describe the loss of the defect's C_{3v} symmetry at the (111)Si/(oxy)nitride interface, we additionally introduce a *distribution in the dangling-bond direction* around a mean direction **l**. This is taken to be described by a Gaussian distribution in χ of mean $\langle\chi\rangle=0$ and standard deviation $\delta\chi$, where χ is defined as the angle between the dangling-bond symmetry axis and **l**. At the (111)Si/(oxy)nitride interface we will assume, at the onset, that **l** coincides with [111], the normal to the (111) interface (see Fig. 10). The model closely resembles the one proposed in Refs. 44 and 47. In the case of the P_b defect in high-T_{ox} ($T_{ox}\gtrsim 850\,^\circ$C) standard (111)Si/SiO$_2$, $\delta\chi\sim 0°$.[44]

For the applied field at an angle ϑ with the normal [111], the derivative line shape of the P_{bN} defect may be calculated as

$$\frac{dP_{\mu a}}{dB}(B,\vartheta)=\int_{-\infty}^{+\infty} V(B-B')K(B',\vartheta)dB' , \qquad (9)$$

where $V(B-B')$ is the field derivative line shape of P_{bN} in the absence of interface strain, while $K(B',\vartheta)dB'$ gives the probability for a P_{bN} defect having a resonance field between B' and $B'+dB'$ at angle ϑ. Contributions to $V(B-B')$ include unresolved dipolar interactions within the P_{bN} system and unresolved hyperfine interactions with ^{29}Si and ^{14}N nuclei. Both interactions are independent of the applied microwave frequency. The line shape of the P_b defects at the conventional (111)Si/SiO$_2$ interface under minimal interface strain has been analyzed in detail.[13,22] As yet, no such study exists for the P_{bN} de-

fect. Therefore, in the present case, $V(B-B')$ is assumed to be a Voigt profile (a convolution of Lorentzian and Gaussian profiles), which is a fair approximation[13,22] of the P_b line shape for a not too large P_b density. $K(B',\vartheta)$ incorporates the broadening introduced into the P_{bN} signal both as a result of the Gaussian *distribution in* $g_\perp$ and, along the present proposal, the site-dependent *tilting of the dangling bond* (χ distribution). Both distributions will introduce a frequency-dependent line broadening. We may approximate $K(B,\vartheta)$ as

$$K(B,\vartheta)=\frac{1}{\sqrt{2\pi}\delta B_\perp}\int_{-\infty}^{+\infty}\exp\left[-\frac{1}{2}\left[\frac{B_\perp-\bar{B}_\perp}{\delta B_\perp}\right]^2\right]\times K_\chi(B,B_\perp,\vartheta)dB_\perp\ , \tag{10}$$

where the exponential function represents the Gaussian distribution in $B_\perp$ (the field corresponding to $g_\perp$) of standard deviation $\delta B_\perp$ around the mean $\bar{B}_\perp$, and $K_\chi(B,B_\perp,\vartheta)$ describes the distribution arising from the tilting effect.

Since we assume equal Gaussian χ distributions in all planes perpendicular to the interface (lateral uniformity), the probability of finding a dangling bond in an infinitesimal solid angle $d\Omega=\sin\chi\, d\chi/2$ is given, for $\mathbf{B}\|[111]$ (i.e., $\vartheta=0$), as

$$K_\chi(\chi)d\chi=\frac{|\sin\chi|}{2\sqrt{2\pi}\delta\chi}\exp\left[-\frac{1}{2}\left[\frac{\chi}{\delta\chi}\right]^2\right]d\chi\ . \tag{11}$$

In Fig. 10 is shown the distribution $K_\chi(\chi)$. Contrary to the P_b defects at the good-quality (111)Si/SiO_2 interface, the maximum of the P_{bN} direction distribution no longer coincides with the [111] axis. In terms of B, we can write

$$K_\chi(B,B_\perp,\vartheta=0)=K_\chi(\chi)\left|\frac{d\cos\chi}{dB}\right|\ , \tag{12}$$

with

$$B(\vartheta=0,\chi)=\frac{h\nu}{\mu_B}\{[g_\parallel\cos\chi]^2+[g_\perp\sin\chi]^2\}^{-1/2}\ . \tag{13}$$

Here h is Planck's constant, ν is the microwave frequency, and μ_B is the Bohr magneton. Combining Eqs. (11)–(13) then leads to

$$K_\chi(B,B_\perp,\vartheta=0)=\frac{1}{\sqrt{2\pi}\delta\chi}\exp\left[-\frac{1}{2}\left[\frac{\chi}{\delta\chi}\right]^2\right]\times\frac{B_\parallel B_\perp^2}{B^2\sqrt{B_\parallel^2-B_\perp^2}\sqrt{B^2-B_\perp^2}}\ , \tag{14}$$

with

$$\chi=\arccos\left[\frac{B_\parallel^2}{B^2}\frac{B^2-B_\perp^2}{B_\parallel^2-B_\perp^2}\right]^{1/2}\ . \tag{15}$$

For the orientations of **B**, where **B** and **l** are not collinear, the resonance field can no longer be expressed in such a compact way. In that case, $K_\chi(B,B_\perp,\vartheta)$ has to be computed numerically using Eqs. (4) and (11).

In Fig. 9 is illustrated a fit to the experimental K-band P_{bN} line shape observed at 4.3 K for $\vartheta=0°$ and 90° using a Voigt profile as convoluting shape [i.e., $V(B-B')$ in (9)]. The fitting results are summarized in Table II. The peak-to-peak linewidths of the Voigt profile and its Lorentzian and Gaussian fractions are represented by ΔB_{pp}^V, ΔB_{pp}^L, and ΔB_{pp}^G, respectively, while ΔB_{pp}^T represents the total width of the calculated P_{bN} profile. In good approximation we assumed ΔB_{pp}^V to be isotropic. Also included in Table II are the X-band calculations using the same set of basic parameters (i.e., $\delta g_\perp$, $\delta\chi$, ΔB_{pp}^L, ΔB_{pp}^G, and ΔB_{pp}^V) and the experimental linewidths at both frequencies (X and K bands). It is clear from Fig. 9 and Table II that there is close agreement between the model and experiment for both **B** orientations ($\vartheta=0°$ and 90°) and microwave frequencies using the same set of parameters throughout. Comparison of the X- and K-band linewidths also illustrates the significant frequency-dependent contribution for $\mathbf{B}\|[111]$. And, as anticipated, this broadening contribution for $\mathbf{B}\|[111]$ results mainly from tilting of the dangling bonds; the Gaussian distribution in $g_\perp$ is of minor importance for $\mathbf{B}\|[111]$.[13] Through the nonlinearity of the transfer function $B(\vartheta)$ and the solid-angle effect, the χ distribution [cf. Eq. (11)], translated into field units, results in distinctly asymmetric line shapes. That is, a long tail appears at the low- and high-field sides of the P_{bN} resonance for the $\mathbf{B}\|[111]$ and $\mathbf{B}\|[11\bar{2}]$ cases, respectively, in agreement with experiment as illustrated in Fig. 9(a) (see also Fig. 8). We believe that this effect is also the reason for the observation of a slightly smaller g anisotropy of the P_{bN} defect as compared to the P_b defect (see Fig. 5): the g matrix of a single P_b and P_{bN} defect might well be identical. The explanation for the shape reversal feature is considered in favor of the present model. Finally, it is important to mention that, apart from the χ distribution, there is a significant contribution of the distribution in $g_\perp$ for $\mathbf{B}\|[11\bar{2}]$. This results in an extra line broadening and attendant lowering of the asymmetry, which are both observed in Fig. 9.

Expanding the above simulation procedure to the sig-

TABLE II. Tabulation of the parameters obtained from fitting the combined simplified dangling bond direction and $g_\perp$ distribution model [cf. Sec. V B] to the P_{bN} line shapes observed for $\vartheta=0°$ and 90° at 4.3 K on (111)Si/Si_3N_4 [cf. Fig. 9(a)]. Experimental linewidths are also included.

	Model							Experiment	
Field direction	$\delta g_\perp$ (10^{-4})	$\delta\chi$ (rad)	ΔB_{pp}^L (G)	ΔB_{pp}^G (G)	ΔB_{pp}^V (G)	$\Delta B_{pp}^T(X)$ (G)	$\Delta B_{pp}^T(K)$ (G)	$\Delta B_{pp}^T(X)$ (G)	$\Delta B_{pp}^T(K)$ (G)
$\mathbf{B}\|[111]$	6.60	0.232	2.55	2.25	3.86	6.19	7.10	6.0±0.1	7.0±0.15
$\mathbf{B}\|[11\bar{2}]$	6.60	0.232	2.55	2.25	3.86	6.67	8.99	6.2±0.1	9.0±0.15

TABLE III. Parameters deduced from fitting the $g_\perp$ and DB direction distribution model to the K-band linewidth anisotropy of P_b and P_{bN} for three samples studied in Fig. 6. For the P_b defect at the (111)Si/SiO$_2$ interface no angular dangling-bond distribution was assumed ($\delta\chi=0°$).

Sample	$\delta g_\perp$ (10^{-4})	$\delta\chi$ (rad)
(111)Si/SiO$_2$	7.20	0
(111)Si/oxynitride (type A)	6.65	0.212
(111)Si/Si$_3$N$_4$ (type B)	5.70	0.190

nals for all ϑ values, one may try a self-consistent fitting of the observed linewidth versus ϑ variations. In Fig. 6 are shown the resulting fits to the K-band linewidth anisotropy data for three samples; that is, the P_b signal in (111)Si/SiO$_2$ and the P_{bN} resonance in (111)Si/oxynitride (sample A) and (111)Si/Si$_3$N$_4$ (sample B). The fit, using the parameters listed in Table III, appears quite satisfactory. The P_{bN} Si/Si$_3$N$_4$ values are in fair agreement with those of Table II. In the case of the P_b defect at the (111)Si/SiO$_2$ interface, no dangling-bond distribution ($\delta\chi=0°$) has been assumed. We again notice that, in contrast to the Si/Si oxide sample, the linewidth anisotropy shows a steep increase for small ϑ and a characteristic maximum for $\vartheta\approx 60°$, both features reassuringly reproduced by the model. We may therefore conclude that the deviating behavior of the P_{bN}'s linewidth anisotropy (as compared to P_b) is caused by the distortion of the axial symmetry of the $\overleftrightarrow{g}$ dyadic.

C. Temperature dependence

When temperature rises, the P_{bN} linewidth starts to decrease for all orientations, as illustrated for sample B in Fig. 7, with attendant fading of the line-shape asymmetry. The high-T P_{bN} line shape is illustrated in Fig. 9(b) for $\mathbf{B}\|[111]$ and $\mathbf{B}\|[11\bar{2}]$. Both spectra appear well symmetric and could be fitted with a Lorentzian profile of $\Delta B^L_{\rm pp}=4.89\pm0.04$ G and a Gaussian shape of $\Delta B^G_{\rm pp}=8.39\pm0.20$ G for $\mathbf{B}\|[111]$ and $\mathbf{B}\|[11\bar{2}]$, respectively. In light of the advanced angular dangling-bond distribution at low T, it seems obvious to attribute the temperature dependence of the linewidth and shape to the collapse of this distribution. Indeed, the linewidth will then decrease and the P_{bN} line shape becomes symmetric for all orientations. The resultant Gaussian shape for $\mathbf{B}\|[11\bar{2}]$ then simply mirrors the Gaussian distribution in $g_\perp$, then dominating the line shape, while the Lorentzian shape observed for $\mathbf{B}\|[111]$, in fact, reflects the absence of frequency-dependent broadening. In the following we will provide evidence that the disappearance of the angular dangling-bond distribution may result from thermally activated reorientations of the defect at higher T.

A major issue in the outlined P_{bN} model is that the lateral off relaxation of the central Si atom leads, for each defect, to differently relaxed configurations, likely of close energy levels, on average separated by an energy barrier ΔE. At low temperatures ($T\approx 4.3$ K in our case) no reorientations occur and the ESR spectrum consists of a superposition of the resonances of all possible P_{bN} configurations. Upon increasing T, transitions between the different off-relaxed configurations become appreciable, thus causing a lifetime broadening on the low-T spectrum. The relationship between T and the characteristic time τ for the thermally activated reorientation of the central Si atom is usually given[42] by an Arrhenius-type relation

$$\tau=\tau_0\exp\frac{\Delta E}{kT}\ , \tag{16}$$

where k is Boltzmann's constant. When the transition rate ($\sim\tau^{-1}$) becomes fast enough, the spectrum reflects an averaged resonant wave function of the different off-relaxed configurations, with the attendant appearance of a narrowed average spectrum—the well-known motional narrowing effect.

According to the theory of Gutowsky and Saika,[55] as applied to paramagnetic defects by Watkins and Corbett,[42] we consider as an example two relaxed P_{bN} configurations P and Q, occurring with equal probabilities and with resonance fields separated by ΔB^*. The low-T spectrum will consist of two lines (P and Q) of equal amplitudes and with linewidths determined by static interactions. With rising temperature the lifetime τ shortens along Eq. (16) due to a thermally activated structural hopping process. When T is such that τ is in the range of $\tau\gamma\Delta B^*\approx 1$, the resonance lines will broaden. Theory predicts that in this range, where the hopping broadening dominates, $T_2=2\tau$, where T_2 is the spin-spin-relaxation time of the homogeneous part of the resonance, and $\gamma=g\mu_B/\hbar$. If the latter part exhibits a Lorentzian shape of width $\Delta B^L_{\rm pp}=2/\sqrt{3}\gamma T_2$, the lifetime τ can be calculated from the hopping-induced broadening as

$$\tau=\frac{1}{\sqrt{3}\gamma\Delta B^L_{\rm pp}}\ . \tag{17}$$

At still higher T, the intersignal jump rate of the spins becomes much larger than the difference in Larmor frequencies of the two resonances, so the loss in phase coherence between jumps becomes insignificant. This condition is met at temperatures where $\tau\gamma\Delta B^*\ll 1$. Another resonance of Lorentzian shape appears in the middle of the broadened signals P and Q, of which the linewidth is predicted to be

$$\Delta B^L_{\rm pp}=\frac{\tau\gamma(\Delta B^*)^2}{2\sqrt{3}}\ . \tag{18}$$

It is clear from this relation that the width of this additional signal, born out of signals P and Q, will narrow with rising T. So the linewidth of the motionally narrowed resonance [Eq. (18)] provides another way to estimate τ.

Some difficulties are met when applying this theory to the temperature dependence of the P_{bN} linewidth. First, instead of two resonance signals (P and Q, as taken as example in the theory), only a single P_{bN} signal is measured,

actually the superposition of the resonance signals for all differently relaxed configurations. The continuous distribution in strain along the interface causes a continuous distribution of relaxed configurations both as regards energy levels and resonance fields. Thus we obtain a continuous distribution of signals, described by the frequency-dependent broadening $K(B,\vartheta)$. In the case of a single P_{bN} defect the probability distribution of the resonance fields of the relaxed states is given by $K(B,B_\perp,\vartheta)$. Hence, instead of a fixed field splitting ΔB^* between the two signals P and Q (theory) of a given P_{bN} defect, we obtain a distribution of field splittings, the average of which may be approximated by ΔB^χ.

A second difficulty concerns the evaluation of the homogeneous part of the linewidth from experimental data. In general, the experimental linewidth comprises a homogeneous part (ΔB^L_{pp}), a part due to unresolved hyperfine interactions, and a frequency-dependent part. As shown, the frequency-dependent part itself contains two contributions, $\Delta B^{g_\perp}_{pp}$ and ΔB^χ_{pp}, resulting from the $g_\perp$ and χ distributions, respectively. The latter contribution is motionally narrowed at higher T. If we neglect the linewidth ΔB^χ_{pp} at higher T, it is feasible to calculate ΔB^L_{pp} from the experimental width ΔB_{pp} and the unresolved hyperfine and $g_\perp$ broadenings, both of which are T independent. If we approximate the latter two by a distribution of width ΔB^0_{pp}, ΔB^L_{pp} is approximately given as $\Delta B^L_{pp}=\Delta B_{pp}-\Delta B^0_{pp}$. Substituting this into Eq. (18) and taking into account that $\Delta B^*\simeq\Delta B^\chi$, for the lifetime τ in case of motional narrowing we obtain

$$\tau=\frac{\sqrt{3}}{\gamma \ln 2}\frac{\Delta B_{pp}-\Delta B^0_{pp}}{(\Delta B^\chi_{pp})^2} . \tag{19}$$

It is possible with Eq. (19) to calculate the hopping rate τ^{-1} of the P_{bN} defect from the temperature dependence of the linewidth. Yet the low-T τ values will deviate from the Arrhenius-type behavior because of the condition $\tau\gamma\Delta B^*\ll 1$ is not fulfilled. On the other hand, a calculation of τ from the linewidth data using Eq. (17) is not feasible because of the difficulty in deriving accurate values for ΔB^L_{pp} at low T. The inhomogeneous part of the low-T P_{bN} linewidth, i.e., the frequency-dependent broadening (both $\Delta B^{g_\perp}_{pp}$ and ΔB^χ_{pp}) and the unresolved hyperfine broadening, dominates the total width, so the width ΔB^L_{pp} of the homogeneous part will be hard to resolve. Moreover, because of the small ΔB^χ_{pp} value, the temperature ranges pertaining to motional broadening and motional narrowing overlap.

Figure 11 shows the lifetime-vs-$1/T$ behavior as calculated from the linewidth data for P_{bN} in (111)Si/Si_3N_4 shown in Fig. 7 using Eq. (19). In this, the parameters ΔB^0_{pp} and ΔB^χ_{pp} have been optimized so as to make the $\ln\tau$-vs-T^{-1} curves converge with rising temperature for both orientations ($\mathbf{B}\|[111]$ and $\mathbf{B}\|[11\bar{2}]$) and microwave frequencies (X and K bands), as required by theory. However, a few restrictions have been imposed in order to obtain unique (and, hopefully, reliable) lifetime data. It has been discussed above that ΔB^0_{pp} for $\mathbf{B}\|[111]$ is dominated by unresolved hf interactions. As this contribution is frequency independent, we obtain the condition $\Delta B^0_{pp}(X)=\Delta B^0_{pp}(K)$ when $\mathbf{B}\|[111]$. In addition, the estimate of the unresolved hf broadening has to agree with other estimates (see Secs. V B and V D). When rotating $\mathbf{B}$ to $\mathbf{B}\|[11\bar{2}]$, ΔB^0_{pp} is additionally enhanced by the distribution in $g_\perp$, from which the condition $\Delta B^0_{pp}(\mathbf{B}\|[111])<\Delta B^0_{pp}(\mathbf{B}\|[11\bar{2}])$ for all microwave frequencies originates. The distribution in $g_\perp$ is frequency dependent, from which we obtain the restriction $\Delta B^0_{pp}(X)<\Delta B^0_{pp}(K)$ when $\mathbf{B}\|[11\bar{2}]$. In the same way, we obtain the condition $\Delta B^\chi_{pp}(X)<\Delta B^\chi_{pp}(K)$ for $\mathbf{B}\|[11\bar{2}]$. An important condition is also imposed by the experimental linewidth at low T, which is the upper limit for both ΔB^0_{pp} and ΔB^χ_{pp}. All restrictions are fulfilled in the fitting procedure.

Figure 11 can be divided into two regions. The lifetimes in region II, as calculated from the temperature dependence of the linewidth for the different $\mathbf{B}$ directions and microwave frequencies, do not coincide. In this region, motional narrowing [Eq. (19)] does not apply. In region I (above 20 K), in contrast, all $\ln\tau$-vs-T^{-1} curves converge to a single straight line, Arrhenius fitting [Eq. (16)] giving $\tau_0=(6.9\pm2.0)\times10^{-10}$ s and $\Delta E=0.006\pm0.001$ eV. These data are consistent with the idea that the reorientation of the P_{bN} center for $T\gtrsim5$ K is dominated by thermal reorientation. From the motional broadening condition it is possible, using the estimates for τ_0 and ΔE, to calculate the threshold temperature T_B,

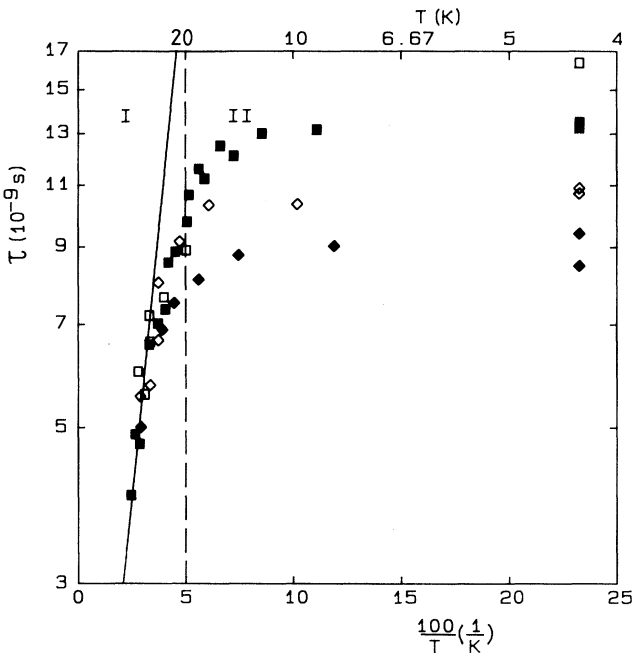

FIG. 11. Lifetime τ, describing the thermally activated P_{bN} reorientation, vs temperature, calculated from the linewidth data shown in Fig. 7, assuming a motional-narrowing regime. Squares and diamonds represent τ values calculated from linewidths measured for $\mathbf{B}\|[111]$ and $\mathbf{B}\|[11\bar{2}]$, respectively. Open and solid symbols refer to X- and K-band measurements, respectively. The solid curve represents an Arrhenius-type fit.

separating regions I and II, giving $T_B \approx 25$ K. The close agreement of the theoretically obtained T_B with the border temperature determined by eye from the shapes of the curves in Fig. 11, supports the model. The small activation energy and the relatively high vibrational frequency factor τ_0^{-1} are suggestive of merely electronic effects rather than of atomic motion, indicating that the central Si atom of the P_{bN} defect remains near the symmetry axis. The fact that no significant shift in the ^{29}Si hf interaction doublet is observed compared to the ^{29}Si hf splitting of the P_b defect at the standard (111)Si/SiO$_2$ interface corroborates this conclusion about the weakness in atomic distortion. It should be remembered, however, that the influence of the electron wave function distortion on the hyperfine splitting is much less important[56] than inferred from simple molecular-orbital calculations.[13,57]

A final remark regards the observation that the P_{bN} spectrum can be easily observed out of saturation down to 4.3 K—quite unusual for the P_b defect in thermal (111)Si/SiO$_2$.[22,46] The outlined interpretation suggests that shorter relaxation times might arise from motional averaging over various weak distortions in the C_{3v} symmetry for P_{bN}. Such anomalous saturation behavior has been observed before in motionally narrowed deep-level defects.[58] It needs to be added, though, that, following a previous suggestion,[18] the highly reduced saturability may also result from an intensified interaction with a nearby conduction-electron bath. So far, this matter remains unclear.

D. Unresolved hyperfine interactions

The natural abundance (ζ_n) of the ^{14}N isotope of $I=1$ is as high as 99.63%. Hence it appears that the P_{bN} defect would represent an excellent case for characterizing the insulator side environment of the interfacial ·Si≡Si$_3$ defect through ESR probing of the ^{14}N hf structure. If sufficiently strong, the interaction of the unpaired electron with one ^{14}N site would result in a triplet ESR pattern composed of three equidistant and equally intense signals. This contrasts with the Si/SiO$_2$ structure, where, because of the fact that the sole magnetic oxygen isotope ^{17}O of $I=\frac{5}{2}$ is only 0.037% abundant, one has recourse to rather cumbersome ^{17}O enrichment procedures to conduct such a study.[59,60]

Unfortunately, however, no resolved ^{14}N hf structure is discernable in the P_{bN} spectra (see, e.g., Fig. 4). This implies that the ^{14}N hf interaction is too weak to surmount the other broadening mechanisms, and, hence, remains hidden as unresolved hf broadening of the signal. This is unlike the P_b case, where a previous study[60] on 51.24% ^{17}O-enriched thermal (111)Si/SiO$_2$ ($T_{ox}=920$ °C) revealed some partially resolved ^{17}O hf structure of splitting $A_{\parallel} \sim 2.7$ G, resulting from interaction with one O site in a first-neighboring shell. This dissimilarity in ^{17}O and ^{14}N hf interaction strength, however, rather than being in conflict, appears to comply with our understanding of hf interactions. At least, it may be made plausible in an idealized view, starting from the basic identity (i.e., interfacial ·Si≡Si$_3$) of the P_b and P_{bN} defects and, somewhat naively, accepting that the crucial neighboring ^{17}O and ^{14}N shell configuration is identical. If we further leave the unpaired electron's wave function nature unaltered, it is then clear from Ref. 48 that the isotropic Fermi-contact hf interaction $A_{\rm iso} \propto |\mu| = g_N \mu_N I$, where g_N and μ_N represent the nuclear g factor and nuclear magneton, respectively. Hence, it is expected that ^{14}N hf interaction will be about $|\mu(^{14}\text{N})/\mu(^{17}\text{O})| = 0.4036/(0.7572 \times \frac{5}{2}) = 0.21$ times weaker than the ^{17}O one, thus explaining the absence of any resolved ^{14}N hf structure.

Further analysis then must try to extract this broadening part from the observed signal width. If successful, it will be interesting to compare with the similar *unresolved* ^{17}O hf part present in the P_b signal, as it may provide information on the relative insulator environment of the respective centers. Separating the ^{14}N hf broadening may appear tough, though, as we have shown that, even when sticking to the simplest case of the $\mathbf{B} \perp (111)\text{Si}/\text{Si}_3\text{N}_4$ interface, the P_{bN} Zeeman resonance contains, beside the unresolved hf broadening due to ^{29}Si and ^{14}N nuclei and the concentration-dependent broadening due to dipolar interactions,[22] a significant strain-induced frequency-dependent contribution for $\mathbf{B} \| [111]$. While this may sound pessimistic, we nevertheless have a few estimates at our disposal from Secs. V B and V C. Indeed, the estimated value $\Delta B_{\rm pp}^{V}$ for the K-band derivative linewidth due to dipolar and unresolved hyperfine broadening for $\mathbf{B} \| [111]$ is 3.86 G (see Table II), as derived from P_{bN} line-shape fitting. The hf contribution $\Delta B_{\rm pp}^{\rm hf}$ of the linewidth can be extracted from $\Delta B_{\rm pp}^{V}$ if the dipolar broadening is known as a function of $[P_{bN}]$. This broadening is taken identical to the P_b dipolar broadening at the (111)Si/SiO$_2$ interface,[22] giving the dipolar broadening $\Delta B_{\rm pp}^{DD} = 0.76 \pm 0.1$ G for $7 \times 10^{12} < [P_{bN}] < 32 \times 10^{12}$ cm^{-2}, from which $\Delta B_{\rm pp}^{\rm hf} \approx \Delta B_{\rm pp}^{V} - \Delta B_{\rm pp}^{DD} = 3.07 \pm 0.1$ G. This hyperfine contribution consists of two parts, i.e., unresolved hyperfine broadening $\Delta B_{\rm pp}^{\rm hf}(^{29}\text{Si})$ with ^{29}Si atoms ($I=\frac{1}{2}$; $\zeta_n = 4.7\%$) and unresolved hyperfine broadening $\Delta B_{\rm pp}^{\rm hf}(^{14}\text{N})$ with ^{14}N atoms. It has been shown previously[22] that unresolved ^{29}Si hf broadening exhibits a maximum peak-to-peak width of maximum 1.29 ± 0.02 G. To extract from this the linewidth due to ^{14}N hf broadening we will use the average of two methods. In the first we assume that both the ^{29}Si and ^{14}N hyperfine distributions are Lorentzian, so that $\Delta B_{\rm pp}^{\rm hf}(^{14}\text{N}) = \Delta B_{\rm pp}^{\rm hf} - \Delta B_{\rm pp}^{\rm hf}(^{29}\text{Si})$. The second approach assumes both broadenings to be Gaussian, so that $\Delta B_{\rm pp}^{\rm hf}(^{14}\text{N}) = [(\Delta B_{\rm pp}^{\rm hf})^2 - (\Delta B_{\rm pp}^{\rm hf}(^{29}\text{Si}))^2]^{1/2}$. While neither of the two approximations will be strictly valid, the average of both results $\Delta B_{\rm pp}(^{14}\text{N}) = 2.28 \pm 0.2$ G will be adequate.

We now turn to the unresolved ^{17}O hf broadening of the P_b signal. The previous K-band study[60] of 51.24% ^{17}O enriched thermal (111)Si/SiO$_2$ unveiled that, apart from some partially resolved structure, a main part of the ^{17}O hf interaction remained unresolved, resulting in a width of the P_b Zeeman resonance $\Delta B_{\rm pp}^{\rm ER} = 2.71 \pm 0.06$ G for $\mathbf{B} \| [111]$. The unenriched sample (0.037% ^{17}O) of equal $[P_b]$ exhibited a width

$\Delta B_{pp}^{U}=1.69\pm0.03$ G, which, in addition to the ^{29}Si induced width $\Delta B_{pp}^{hf}(^{29}\text{Si})$, also contains a small dipolar part ΔB_{pp}^{DD}.[22] Carrying out a similar derivation as applied above to the ^{14}N P_{bN} case leads to $\Delta B_{pp}^{hf}(^{17}\text{O})=1.57\pm0.06$ G.

It then remains to compare both unresolved hf broadenings $\Delta B_{pp}^{hf}(^{14}\text{N})$ and $\Delta B_{pp}^{hf}(^{17}\text{O})$ in terms of relative isotopic surrounding. Perhaps the most lucid way to do this is by analyzing what might be expected for the ratio of the unresolved hf broadening $R_{hf}\equiv\Delta B_{pp}^{hf}(^{14}\text{N})/\Delta B_{pp}^{hf}(^{17}\text{O})$ for the case where the capping environments of P_b and P_{bN} would configurationally be fully identical, except regarding the nuclear properties of the ^{17}O and ^{14}N isotopes. In doing this, we will make the reasonable assumption that, considering the high fractional abundance ζ of magnetic isotopes (~1), $\Delta B_{pp}^{hf}\propto\sqrt{\zeta\rho}$ (see, e.g., Refs. 48 and 61). We then expect

$$R_{hf}\sim\frac{|\mu(^{14}\text{N})|\sqrt{\zeta(^{14}\text{N})\rho(\text{N-sites})}}{|\mu(^{17}\text{O})|\sqrt{\zeta(^{17}\text{O})\rho(\text{O-sites})}}=0.33\ , \tag{20}$$

where ρ represents the volume density of pertinent sites. Clearly, the prediction deviates from the experimental R_{hf} value of 1.45 ± 0.18. There is, however, one obvious additional complication. In the case of P_{bN}, the hemispherical cloud of all interacting N sites contributes to the unresolved ΔB_{pp}^{hf}—there is no resolved part. This is unlike the ^{17}O P_b situation, where the strongest hf interaction (with one O site) is partially resolved. Roughly stated, only two-sixths of this interaction remain embedded in the central signal (see, e.g., Ref. 60; $A_{\parallel}\sim2.7$ G vis à vis $\Delta B_{pp}^{ER}=2.71$ G). If P_{bN} would endure a similar strongest hf interaction with only one ^{14}N site in a first shell, ideally only two-thirds of the interaction would contribute to $\Delta B_{pp}^{hf}(^{14}\text{N})$. This would thus result in raising relation (20) roughly by a factor ~2, bringing it closer to the experiment.

The remaining difference may be interpreted in various ways. Part of it may be due to the implicit assumption made that the hf broadening line shapes are identical in both cases, which may be violated for different I values, i.e., ^{17}O ($I=\frac{5}{2}$) and ^{14}N ($I=1$). More physically, on the other hand, it may refer to a likely dissimilarity in the P_b and P_{bN} cappings, i.e., Si—O and Si—N bond lengths, atomic positioning, etc. It is unfortunate that, even when backed up by reliable, accurate theoretical hf calculations of P_b and P_{bN} models, the lack of any resolved hf structure in the P_{bN} spectra will prevent us from clarifying that difference via the classical ESR way. Perhaps ESR observations at sufficiently low frequency, where marring g-spread broadenings will collapse, may be more successful.

The first overall conclusion, however, is that the derived unresolved hf broadenings, stemming from the hemispherical clouds of ^{17}O and ^{14}N interacting sites, mutually comply with the known isotopic properties. Second, like the ^{17}O P_b case, the ^{14}N P_{bN} hf splitting is found to be small—in effect, no resolved hf structure is observed; this complies with the accepted P_b and P_{bN} models (i.e., interfacial $\cdot\text{Si}\equiv\text{Si}_3$), as in neither case is N or O seen as an immediate part of the defect structure.

VI. CONCLUSIONS

Silicon (oxy)nitride films, 31 ± 3 Å thick, have been thermally grown on (111)Si in pure NH_3 for 100–200 min in the range 1000–1150 °C. An important finding is that stoichiometric Si_3N_4 layers are only obtained when *in situ* removing any initial oxide layers (e.g., native oxide) prior to nitridation. XPS analysis showed these Si_3N_4 films to be uniform except for the top layer, which is contaminated with adsorbed O and C species.

Upon dehydrogenation, ESR studies revealed the existence of two defects. A first one, of isotropic $g=2.0028$ and inhomogeneously broadened linewidth ΔB_{pp} (K band) $=6.3\pm0.8$ G, could be detected in stoichiometric nitrides only. It was found to be uniformly distributed over the film with concentrations $\sim2.3\times10^{17}$ cm^{-3}. It is identified with the K center, a dangling bond on a Si atom, backbonded to three N atoms. The second defect, called P_{bN} (with $g_{\parallel}=2.001\,49\pm0.000\,03$ and $g_{\perp}=2.008\,52\pm0.000\,07$ for Si/Si_3N_4) was identified as the counterpart of the P_b defect at the (111)Si/SiO_2 interface, i.e., a singly occupied Si orbital on an interfacial Si atom, backbonded to three Si atoms in the substrate, and pointing in the [111] direction. It is observed both in the (111)Si/oxynitride and Si/Si_3N_4 structures. The identification of the defect stems from various striking similarities with the P_b defect, such as are the $\overleftrightarrow{g}$ dyadic, the linewidth anisotropy, and the ^{29}Si hf interaction. From this is concluded that the salient features of the interfacial $\cdot\text{Si}\equiv\text{Si}_3$ defect are mainly set by the underside Si matrix and not so much by the nature of the top insulator.

But, as expected, there also appear typical differences (albeit on a second level) in some ESR properties (such as concentration, line shape and linewidth, temperature dependence, and saturation behavior) of both defects, which do refer to the dissimilarities between the overlaying Si (oxy)nitride and Si oxide films. The rigidity of the Si (oxy)nitride basic structure as compared to Si oxide necessitates more dangling bonds to relieve the interface stress leading to an increased P_{bN} concentration. The latter varies in the range $N_S=(7-32)\times10^{12}$ cm^{-2}, depending on the dehydrogenation treatment.

Owing to the increased interface strain, the symmetry of part of the P_{bN} defects is weakly perturbed with respect to the P_b's C_{3v} symmetry, mainly by a relaxation away from the symmetry axis of the central Si atom in the defect. A model describing the impact of the relaxation as an effective tilting of the $\overleftrightarrow{g}$ dyadic symmetry axis—and thus of the dangling bond—may account for the characteristic behavior of the linewidth anisotropy, the frequency-dependent contribution to the width, the line-shape asymmetry, and the shape reversal feature at 4.3 K.

The deviations of these parameters relative to the P_b defect at the (111)Si/SiO_2 interface gradually disappear with increasing T due to thermally activated hopping of the defect over the various off-relaxed configurations.

The energy barrier for the reorientation ΔE is found to be 0.006 ± 0.001 eV. This motional narrowing over the P_{bN} defect distortions may also partly account for the strongly reduced low-T saturatibility of P_{bN} as compared to P_b.

From the fit of the model to the low-T P_{bN} line shape for $\mathbf{B}\|[111]$ and $\mathbf{B}\|[11\bar{2}]$, and the calculation of the T dependence of the linewidths, the approximate value 3.83 ± 0.10 G is obtained for the P_{bN} resonance linewidth at the (111)Si/Si$_3$N$_4$ interface in the absence of strain broadening. In turn, this leads to an approximate value of 2.28 ± 0.2 G for the width of the unresolved hyperfine broadening due to interaction of the P_{bN} paramagnetic electron with ^{14}N nuclei in the top Si$_3$N$_4$ film.

Comparison of the ^{17}O and ^{14}N unresolved hf broadening of the P_b and P_{bN} defects, respectively, shows these to comply with the known magnetic properties of these isotopes. The results confirm the $P_{b(N)}$ defect as a prototype *dangling* bond highly localized on a threefold-coordinated Si atom at the interface, counter to the previously proposed floating bond model.[62]

[1]S. M. Sze, J. Appl. Phys. **38**, 2951 (1967).

[2]T. Ito, T. Nakamura, and H. Ishikawa, IEEE Trans. Electron Devices ED-**29**, 498 (1982).

[3]R. Hezel, Radiat. Eff. **65**, 101 (1982).

[4]S. P. Murarka, C. C. Chang, and A. C. Adams, J. Electrochem. Soc. **126**, 996 (1979).

[5]D. Frohman-Bentchkowsky and M. Lenzlinger, J. Appl. Phys. **40**, 3307 (1969).

[6]P. C. Arnett and B. H. Yun, Appl. Phys. Lett. **26**, 94 (1975); H. Maes and R. J. Van Overstraeten, *ibid.* **27**, 282 (1975).

[7]P. M. Lenahan and S. E. Curry, Appl. Phys. Lett. **56**, 157 (1990).

[8]W. L. Warren, P. M. Lenahan, and S. E. Curry, Phys. Rev. Lett. **65**, 207 (1990).

[9]W. L. Warren, J. Kanicki, F. C. Rong, and E. H. Poindexter, J. Electrochem. Soc. **139**, 880 (1992).

[10]D. T. Krick, P. M. Lenahan, and J. Kanicki, J. Appl. Phys. **64**, 3558 (1988).

[11]G. J. Gerardi, E. H. Poindexter, P. J. Caplan, and N. M. Johnson, Appl. Phys. Lett. **49**, 348 (1986).

[12]See, e.g., E. H. Poindexter and P. J. Caplan, Prog. Surf. Sci. **14**, 201 (1983), and references therein. For a recent review, see the series of papers in Semicond. Sci. Technol. **4**, 961 (1989).

[13]K. L. Brower, Phys. Rev. B **33**, 4471 (1986).

[14]K. L. Brower, Appl. Phys. Lett. **43**, 1111 (1983).

[15]W. E. Carlos, Appl. Phys. Lett. **50**, 1450 (1987).

[16]G. J. Gerardi, E. H. Poindexter, P. J. Caplan, and N. M. Johnson, Appl. Phys. Lett. **49**, 348 (1986); S. T. Chang, J. K. Wu, and S. A. Lyon, *ibid.* **48**, 662 (1986).

[17]A. Stesmans, Appl. Phys. Lett. **48**, 972 (1986).

[18]A. Stesmans, Appl. Surf. Sci. **30**, 134 (1987).

[19]With natural interfaces, we refer to those interfaces as, for example, the thermally grown Si/SiO$_2$ or Si/Si$_3$N$_4$ interfaces. The top Si layers, while being consumed, are incorporated in the grown Si compound cover, as distinct from bilayer formation by straight deposition, such as evaporation, sputtering, glow discharge deposition, etc. A natural Si/solid structure may be expected to exhibit a reproducible, inherent interface structure reflecting the lattice-to-lattice matching constraints.

[20]A. Stesmans and G. Van Gorp, Phys. Rev. B **39**, 2864 (1989); Appl. Surf. Sci. **39**, 317 (1989).

[21]A. Stesmans and J. Braet, Surf. Sci. **172**, 389 (1986).

[22]G. Van Gorp and A. Stesmans, Phys. Rev. B **42**, 3765 (1990); **45**, 4344 (1992).

[23]A. Stesmans, J. Magn. Res. **76**, 14 (1988); A. Stesmans and Y. Wu, J. Phys. D **21**, 1205 (1988).

[24]A. Stesmans and G. Van Gorp, Phys. Lett. A **139**, 95 (1989).

[25]F. H. Habraken, A. E. Kuiper, A. v. Oostrom, Y. Tamminga, and J. B. Theeten, J. Appl. Phys. **53**, 404 (1982).

[26]F. J. Himpsel, F. R. McFeely, A. Taleb-Ibrahimi, J. A. Yarmoff, and G. Hollinger, Phys. Rev. B **38**, 6084 (1988).

[27]R. Kärcher, L. Ley, and R. L. Johnson, Phys. Rev. B **30**, 1896 (1984).

[28]C. M. M. Denisse, J. F. M. Janssen, F. H. Habraken, W. F. Van der Weg, and E. G. P. Schuivens, J. Appl. Phys. **62**, 832 (1982).

[29]J. N. Chiang and D. W. Hess, J. Appl. Phys. **67**, 6851 (1990).

[30]L. Kubler, R. Haug, F. Ringeisen, and A. Jaegle, J. Non-Cryst. Solids **54**, 27 (1983).

[31]T. A. Carlson and G. E. McGuire, J. Electron Spectrosc. **1**, 161 (1972/73).

[32]M. Klasson, A. Berndtsson, J. Hedman, R. Nilson, R. Nyholm, and C. Nordling, J. Electrochem. Soc. **125**, 601 (1978).

[33]A. K. Sinha, H. J. Levinstein, T. E. Smith, G. Quintana, and S. E. Haszko, J. Electrochem. Soc. **125**, 601 (1978).

[34]M. P. Seah and W. A. Dench, Surf. Interf. Anal. **1**, 2 (1979).

[35]C. Maillot, H. Roulet, and G. Dufour, J. Vac. Sci. Techol. B **2**, 316 (1984); J. A. Wurzbach, F. J. Grunthaner, and J. Maserjian, *ibid.* **20**, 962 (1982).

[36]R. Flitsch and S. I. Raider, J. Vac. Sci. Technol. **12**, 305 (1975); J. M. Hill, D. G. Royce, C. S. Fadley, L. F. Wagner, and F. J. Grunthaner, Chem. Phys. Lett. **44**, 225 (1976).

[37]Y. Hayafuji and K. Kajiwara, J. Electrochem. Soc. **129**, 2102 (1982).

[38]S. Yokoyama, M. Hirose, and Y. Osaka, Jpn. J. Appl. Phys. **20**, L35 (1981).

[39]S. Fujita and A. Sasaki, J. Electrochem. Soc. **132**, 398 (1985).

[40]A. Marimoto, Y. Tsujimura, M. Kumeda, and T. Shimizu, Jpn. J. Appl. Phys. **24**, 1394 (1985).

[41]N. Ishii, S. Oozora, M. Kumeda, and T. Shimizu, Phys. Status Solidi B **114**, K111 (1982).

[42]G. D. Watkins and J. W. Corbett, Phys. Rev. **134**, A1359 (1964).

[43]A. Stesmans and G. Van Gorp, Appl. Phys. Lett. **57**, 2663 (1990).

[44]A. Stesmans, Phys. Rev. B **48**, 2418 (1993).

[45]S. Shimoda, I. Shimizu, and M. Migitaka, Appl. Phys. Lett. **52**, 1068 (1988).

[46]K. L. Brower, Phys. Rev. B **38**, 9657 (1988).

[47]A. Stesmans and J. Braet, in *Insulating Films on Semiconductors,* edited by J. J. Simonne and J. Buxo (North-Holland, Amsterdam, 1986), p. 25.

[48]In the simple local-hybrid atomic-orbital picture, the localization (η^2) and hybridization (α^2,β^2) parameters are generally

derived from the experimentally observed isotropic ($A_{\rm iso}$) and anisotropic ($A_{\rm aniso}$) hyperfine splitting constants using the expressions

$$A_{\rm iso}=\tfrac{2}{3}\mu_0 g_0 \mu_B g_N \mu_N \eta^2 \alpha^2 |\Psi_{3s}(0)|^2 ,$$

$$A_{\rm aniso}=\frac{\mu_0}{4\pi} g_0 \mu_B g_N \mu_N \eta^2 \beta^2 \langle r_{3p}^{-3} \rangle ,$$

and the condition $\alpha^2+\beta^2=1$. In these relations, μ_0 is the permeability, μ_N the nuclear magneton, and g_N the g value of the magnetic nucleus. It is clear that the values η^2, α^2, and β^2 will depend on the used (tabulated) values $|\Psi_{3s}(0)|^2$ and $\langle r_{3p}^{-3} \rangle$ of the $3s$ and $3p$ atomic Si orbitals, which are determined by Hartree-Fock calculations on an isolated Si atom or ion. In the work on the P_b defect, the values of Ref. 49 were always used. Other values, however, may lead to distinctly different values for η^2. The hybridization ratio β^2/α^2, on the other hand, remains almost constant because the theoretical estimates of $|\Psi(0)|^2$ and $\langle r_{3p}^{-3} \rangle$ in the different theoretical estimates are positively correlated. Using the values of Ref. 50, for example, leads to $\eta^2=0.60$, $\alpha^2=0.11$, and $\beta^2=0.89$.

[49]D. G. Griffin, R. D. Cowan, and K. L. Andrew, Phys. Rev. A **3**, 1233 (1971).

[50]J. R. Morton and K. F. Preston, J. Magn. Res. **30**, 577 (1978).

[51]These data were derived assuming the defect orbital population and the net spin population to be identical. While this is not true in general (see Refs. 52 and 53), it may serve as an adequate approximation for the present purpose, certainly in light of the uncertainties introduced as described in Ref. 48.

[52]M. Cook and C. T. White, Phys. Rev. Lett. **59**, 1741 (1987).

[53]A. H. Edwards, Phys. Rev. B **36**, 9638 (1987).

[54]The symmetry breaking will cause a lowering of the C_{3v} symmetry so that $g_2=g_3=g_\perp$ no longer holds. But the differences between g_2 and g_3 will be small and site dependent so that, over the set of all P_b's, these variations may effectively be included in a distribution in $g_\perp$ of a still axially symmetric g tensor. This description is adopted in the present model.

[55]H. S. Gutowsky and A. Saika, J. Chem. Phys. **21**, 1688 (1953).

[56]A. H. Edwards, W. B. Fowler, and F.J. Feigl, Phys. Rev. B **37**, 9000 (1988).

[57]D. L. Griscom, E. J. Friebele, and G. H. Sigel, Jr., Solid State Commun. **15**, 479 (1974).

[58]K. L. Brower, Phys. Rev. Lett. **44**, 1627 (1980).

[59]K. L. Brower, Z. Phys. Chem. Neue Folge **151**, 177 (1987).

[60]A. Stesmans and K. Vanheusden, Phys. Rev. B **44**, 11 353 (1991).

[61]G. Feher, Phys. Rev. **114**, 1219 (1959).

[62]S. T. Pantelides, Phys. Rev. Lett. **57**, 2979 (1986).